



Steering the oxygen reduction reaction pathways of N-carbon hollow spheres by heteroatom doping

Jiarun Cheng^{a,1}, Chaojie Lyu^{a,1}, Hangren Li^b, Jiwen Wu^a, Yue Hu^a, Bin Han^a, Kaili Wu^a, Mirabbos Hojamberdiev^c, Dongsheng Geng^{a,d,*}

^a Beijing Advanced Innovation Center for Materials Genome Engineering, Beijing Key Laboratory for Magneto-Photoelectrical Composite and Interface Science, School of Mathematics and Physics, University of Science and Technology Beijing, Beijing 100083, China

^b Institute for Advanced Materials Technology, University of Science and Technology Beijing, Beijing 100083, China

^c Institut für Chemie, Technische Universität Berlin, Straße des 17. Juni 135, 10623 Berlin, Germany

^d School of Materials Science and Engineering, University of Science and Technology Beijing, Beijing 100083, China

ARTICLE INFO

Keywords:

Oxygen reduction reaction
Selectivity
Hollow mesoporous carbon spheres
Heteroatom doping
Electronic structure

ABSTRACT

An original strategy was reported to manipulate ORR selectivity of N-doped hollow mesoporous carbon spheres (N-HMCS) via heteroatom (P and S) doping. Heteroatom doping can not only modulate electronic structure of N-HMCS and proportion/configuration of doped N, but also regulate ORR pathway. Specifically, rich-graphitic N sites and electron-rich C–P bond domains in N,P-HMCS act as electron donors, making *OOH more unstable and easier to desorb into H₂O₂. This severely distorts the sp² lattice of graphene, catalyzing a two-electron ORR synergistically. Conversely, a strong interaction between electron-deficient C–S bond domain and *OOH intermediate due to the introduction of highly electronegative S hinders the desorption of *OOH, leading to the breakage of the O–O bond and promoting four-electron ORR along with the rich-pyridinic N receptor site. The reaction activity and kinetics mechanism present a positive correlation with proportion of graphitic N, revealing graphitic N is the primary active site with a much faster electron transfer capacity.

1. Introduction

Oxygen reduction reaction (ORR) is a significant reaction in the cathodic process of renewable energy conversion devices and commercial electrochemical synthesis [1,2]. ORR is a complex multi-electron reaction involving two competing processes. O₂ can be completely reduced to H₂O via a four-electron pathway or partially to H₂O₂ via a two-electron pathway [3,4]. The former ensures the maximum energy conversion efficiency of fuel cells and metal-air cells, while the latter provides a promising method for the environmentally safe and sustainable on-site electroproduction of H₂O₂ commodity [5–7]. For a long time, the platinum group metals and their alloys, including Pt, Pd, Pt–Hg, Pd–Hg, etc., have been considered as the best electrocatalysts for both reaction pathways [8–11]. While the high price, scarcity, and poor durability of noble-metal-based electrocatalysts seriously impede their large-scale application. Hence, it is inevitable to exploit alternative electrocatalysts to noble-metal-based electrocatalysts with a simple

strategy for understanding the mechanism of the ORR pathway and improving its efficiency for future application.

In recent years, carbon-based materials have obtained extensive attention owing to their typical electronic and geometric structures, special adsorption behavior, and tunable catalytic properties [12,13]. However, the intrinsic weak interaction between pristine carbon materials with oxygen-containing intermediates generally leads to inferior ORR activity and selectivity. Heteroatom doping is a promising approach that can regulate the binding energy by modulating the electronic structure of carbon materials, allowing to customize the ORR pathway selectively. Typically, for N-doped carbon catalysts, the π -conjugated system within the carbon framework can be adjusted by the highly electronegative N atoms, resulting in the redistribution of charges to influence the adsorption energy of intermediates, ORR activity, and selectivity [14]. In general, the doped N atoms exist in the form of pyridinic N, pyrrolic N, graphitic N, and N oxides. Among them, pyridinic N and graphitic N have been discussed extensively as the active

* Corresponding author at: Beijing Advanced Innovation Center for Materials Genome Engineering, Beijing Key Laboratory for Magneto-Photoelectrical Composite and Interface Science, School of Mathematics and Physics, University of Science and Technology Beijing, Beijing 100083, China.

E-mail address: dgeng@ustb.edu.cn (D. Geng).

¹ The authors contributed equally to this work.

<https://doi.org/10.1016/j.apcatb.2023.122470>

Received 29 October 2022; Received in revised form 4 January 2023; Accepted 11 February 2023

Available online 13 February 2023

0926-3373/© 2023 Elsevier B.V. All rights reserved.

sites for ORR process. It is generally considered that graphitic N may be the key factor for enhancing the catalytic activity [15], while the role of pyridinic N lies in the transformation of the two-electron into four-electron ORR mechanism [14,16,17]. Contreras et al. noted a positive shift of ORR onset potential with the increase of graphitic N proportion in N-doped carbon nanotubes and found that the two-electron ORR pathway may be dominant in the carbon nanotubes with high graphitic N content due to more stable formation of H_2O_2 than O_2 adsorption on the graphitic N site [18]. Colavita's group reported that the selectivity toward a four-electron pathway is strongly influenced by the graphitic N/pyridinic N site composition. The weak adsorption of *OOH or H_2O_2 intermediates on the pure graphitic N-doped or pyridinic N-doped graphene cluster models may lead to preferential desorption before the complete reduction of four electrons to H_2O [19]. Hence, controlling the content and configuration of N for a well-defined ORR pathway remains a challenge.

However, the improvement of ORR catalytic activity and selectivity of carbon-based materials by relying alone on N doping is limited because of low onset potential, low limiting diffusion current density, as well as insignificant electron transfer number. Therefore, the binary and ternary heteroatom (B, F, P, and S) doping strategies have become a promising way to further improve the ORR catalytic activity of N-doped carbon-based electrocatalysts [15,20]. Multiple heteroatom doping can not only introduce more defects and edge active sites but form new electron configurations, which enhances the ORR catalytic activity synergistically by a defined ORR pathway. The electronegativity values of re-doped P (2.19) and S (2.58) atoms are remarkably different from that of the C (2.55) and N (3.04) atoms [21,22]. Hence, the P-modification of N-doped carbon-based materials can further change the charge uniformity of the carbon lattice, generating more structural defects as active sites and increasing electron delocalization. Meantime, the S-modification of N-doped carbon-based materials can further increase asymmetric spin and polarizability of carbon atoms and the edge active sites. For instance, the N,P-codoped carbon exhibited an excellent ORR activity than the single N-doped and undoped samples [23]. The N,S co-doped porous carbon was favorable for the positive onset potential and increased the diffusion limited current density relative to those of the unit N-doped carbon [24]. In recent years, many studies have identified the importance of a synergistic effect of heteroatom codoping in boosting ORR activity and promoting the four-electron transfer pathway [25,26]. However, it has also been reported that H_2O_2 is generated via the two-electron pathway of ORR on unitary P-doped carbon nanotubes (P-CNTs) [27]. The P/N co-doped carbon exhibited the lowest energy barrier for enhancing the two-electron ORR, given by the edged P atoms with co-functionalization of O and N sites [28]. Thus, we aim at gaining insights into the effect of different heteroatoms on inducing the change in the N configuration and ORR selectivity of N-doped carbon-based catalysts.

In addition, the hollow structure has been widely studied and applied in many fields given by their advantages of lower density, larger surface area, adjustable void space, and higher structural permeability compared to dense structures [29–31]. The adjustable void space can provide unique nanocavities for reactant molecules and reaction intermediates, and the high permeability of gas and liquid in this void space also accelerates the mass transfer between electrolyte and reactant, improving the catalytic reaction process.

Inspired by the above, we focus on optimizing the activity and selectivity of carbon-based electrocatalysts towards ORR through heteroatom doping, morphology-controlling, and structure-modulating approach. Here, a self-template strategy is developed to integrate N,P and N,S codoping with structural defects and hollow porosity. As expected, the N-doped hollow mesoporous carbon spheres (N-HMCS) are gained by pyrolyzing polydopamine hydrochloride on the surfaces of SiO_2 spheres and sacrificing the template by etching. Subsequently, the phosphorization or sulfurization process of N-HMCS is followed to introduce the second heteroatom for obtaining the N,P codoped HMCS

or N,S codoped HMCS. P and S doping not only increases the defect sites but changes the N content and electronic structure. The graphitic N content increases when P is introduced to N-HMCS, which triggers the two-electron transfer pathway of ORR together with the C–P bond. Meanwhile, N,S codoping increases the pyridinic N content which promotes the four-electron ORR pathway with the C–S bond synergistically. Hence, the difference in the electronic structure caused by heteroatom doping can lead to various chemical rearrangements after the first electron transfer to O_2 , which in turn affects the four-electron/two-electron selectivity of the reaction. Moreover, the N,P- and N,S-codoped HMCS catalysts exhibit a significantly enhanced ORR activity compared to N-HMCS, indicating the positive correlation of ORR activity with the content of graphitic N. This study sheds light on the synergistic effect of these active sites in the hollow structure for improving the activity and selectivity of the ORR.

2. Experimental section

2.1. Materials and synthesis

2.1.1. Chemicals and reagents

Tetraethyl orthosilicate (TEOS, 98%), dopamine hydrochloride (DA, 98%), sodium hypophosphite (NaH_2PO_2 , 99%), sulfur (99%), sodium hydroxide (NaOH, 98%), ethanol (99%), $\text{NH}_3\cdot\text{H}_2\text{O}$ (25–28 wt%), and potassium hydroxide (KOH, 90%) were purchased from Aladdin Reagent Co., Ltd. Ultra-pure water was used in the entire experimental course.

2.1.2. Synthesis of SiO_2 @PDA

N-doped hollow mesoporous carbon spheres (N-HMCS) were prepared using SiO_2 nanospheres (200 nm) as the template [1]. Typically, TEOS (3.8 mmol) was dissolved to the mixed solution of ethanol (23 mL), ultra-pure water (4.3 mL), and $\text{NH}_3\cdot\text{H}_2\text{O}$ (0.6 mL) under vigorous stirring at 25 °C for 1.5 h. The SiO_2 nanospheres were centrifuged and washed several times with ultra-pure water and ethanol, and dried overnight at 50 °C. The SiO_2 nanospheres (100 mg) were transformed into the mixed solution of ultra-pure water (20 mL) and ethanol (80 mL) under sonication for 15 min. Then, dopamine hydrochloride (200 mg) and $\text{NH}_3\cdot\text{H}_2\text{O}$ (1 mL) were added into the solution to polymerize DA on SiO_2 surfaces at 40 °C for 24 h with vigorous stirring. The resultant suspension was centrifuged and washed with ultra-pure water and ethanol. Eventually, the brown-colored precipitate of SiO_2 @PDA was obtained by freeze-drying.

2.1.3. Synthesis of N,P-codoped HMCS (N,P-HMCS) and N,S-codoped HMCS (N,S-HMCS)

100 mg of the as-synthesized SiO_2 @PDA was carbonized to obtain N, C- SiO_2 under Ar at 900 °C for 2 h. After removal of SiO_2 template using 4 M NaOH aqueous solution at 80 °C for 24 h and subsequent N-HMCS collected by wash and centrifugation for several times. Then, 20 mg of N-HMCS was mixed with 200 mg of NaH_2PO_2 and subjected to phosphorization in Ar at 900 °C for 2 h to gain N,P-codoped hollow mesoporous carbon spheres (N,P-HMCS). Note that N,P-HMCS was centrifuged and washed for three times with ultra-pure water and ethanol to ensure its purity. N,S-codoped HMCS (N,S-HMCS) were prepared by following the same procedure applied for the synthesis of N,P-HMCS by replacing NaH_2PO_2 with sulfur powder.

2.2. Electrochemical measurements

The electrochemical performance of ORR was tested under typical three-electrode cell at room temperature in oxygen-saturated 0.1 M KOH solution with Hg/HgO reference electrode, and platinum piece counter electrode. Glassy-carbon (GC) electrode of rotating ring-disk electrode (RRDE, disk electrode area - 0.2475 cm^2 , platinum ring electrode - 0.1866 cm^2 , PINE Research Instrumentation) and rotating disk electrode

(RDE, the electrode area - 0.196 cm², PINE Research Instrumentation) loaded with the synthesized catalysts were used as the working electrode. Specifically, 1 mg of electrocatalyst was dispersed in 78 μ L of ultra-pure water, 20 μ L of isopropanol, and 4 μ L of 5 wt% Nafion solution, and 10 μ L of the catalyst ink subsequently dropped on RRDE followed by air drying to obtain the electrode with the catalysts loading about 400 μ g•cm⁻². All potential values were converted to reversible hydrogen electrode (RHE) by Eq. 1:

$$E_{RHE} = E_{H_2/H_2O} + 0.098 + 0.059pH \quad (1)$$

The ORR polarization curves were obtained by linear scanning voltammetry (LSV) between 1.1 V and 0 V vs. RHE with the scan rate of 5 mV s⁻¹. And the current was subtracted with the background tested in N₂-saturated solution. The ring voltage was fixed at 1.2 V vs. RHE to ensure fast and complete oxidation of H₂O₂ diffusing from the disk electrode. The Tafel diagram was evaluated with the RRDE experimental data for different catalysts. The electron transfer number (*n*) and H₂O₂ selectivity were estimated by Eqs. 2 and 3:

$$n = 4 \times \frac{I_d}{I_d + \frac{I_r}{N}} \quad (2)$$

$$H_2O_2\% = \frac{200 \times \frac{I_r}{N}}{I_d + \frac{I_r}{N}} \quad (3)$$

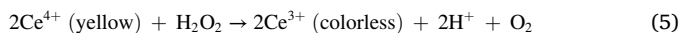
Here, *I_r*, *I_d* and *N* are the ring electrode current, disk electrode current and ring electrode collection efficiency (0.37). In addition, the H₂O₂ selectivity and *n* of catalysts based on RDE were estimated via Koutecký-Levich (K-L) equation (Eq. 4) from polarization curves at different rotation speeds:

$$\frac{1}{j} = \frac{1}{j_k} + \frac{1}{j_L} = -\frac{1}{nFKC_{O_2}} - \frac{1}{0.2nFD_{O_2}^{2/3}v^{-1/6}C_{O_2}\omega^{1/2}} \quad (4)$$

Here, *j*, *j_k* and *j_L* are the current density, kinetic current density and diffusion-limited current density, respectively, which are evaluated based on the K-L Eq. 4, and *n*, *F*, *C_{O₂}*, *D_{O₂}*, *v* and ω are the transferred electron number per O₂, faraday constant (96485 C mol⁻¹), O₂ bulk concentration (1.20 × 10⁻³ M), O₂ diffusion coefficient (1.90 × 10⁻⁵ cm² s⁻¹), kinematic viscosity of solution (0.01 cm² s⁻¹) and electrode rotation rate. And constant 0.2 is given as the rotation speed is indicated by rpm.

2.3. Concentration measurement and faradaic efficiency of H₂O₂ production

The faradaic efficiency (FE) of H₂O₂ generation was assessed via dividing the H₂O₂ production rate performed out 0.1 M KOH solution by the total charge passing through the chronoamperometric method. To further confirm the H₂O₂ selectivity of the N,P-HMCS electrocatalyst, a 45-mL electrolyte in the H-cell with Nafion 117 membrane was used. Catalysts were loaded on Teflon-treated carbon papers (100 μ g cm⁻²), as well as working electrode potential was set up on a applied potential. With the chronoamperometric experiment for 1 h, the quantification of H₂O₂ generated was determined by a traditional Ce(SO₄)₂ titration method according to Eq. 5:



Interestingly, yellow Ce⁴⁺ could be reduced by H₂O₂ to colorless Ce³⁺ through the reaction in Eq. 5. Therefore, the moles of H₂O₂ produced can be determined by measuring the moles of Ce⁴⁺ consumed. The remaining part of Ce⁴⁺ after the reaction was detected using UV-Vis spectroscopy. The consumed charge for H₂O₂ electroproduction (*Q_{H₂O₂}*) can be obtained using Eq. 6:

$$Q_{H_2O_2} = nH_2O_2 \times F \quad (6)$$

Here, *F* is the faraday constant. The total charge (*Q_{total}*) through the

chronoamperometric method for 1 h was carried out by subtracting the charge detected in Ar-saturated 0.1 M KOH in O₂-saturated 0.1 M KOH and it subsequent be estimated by Eq. 7:

$$Q_{total} = \int idt \quad (7)$$

Thus, the FE of H₂O₂ electroproduction can be followed:

$$FE = \frac{Q_{H_2O_2}}{Q_{total}} \times 100\% \quad (8)$$

2.4. Theoretical study

All density functional theory (DFT) calculations were performed using the plane-wave CASTEP package in our work [32,33]. The generalized gradient approximation (GGA) with the Perdew-Burke-Ernzerhof (PBE) was used to treat the exchange and correlation potentials [34]. The kinetic cutoff energy for the plane-wave expansion was fixed at 500 eV for the bulk and surface. The adsorption of O₂ and *OOH on the surfaces of N,P- and N,S-codoped HMCS-based materials was studied using the CASTEP package. A 6 × 3 × 1 supercell of graphene was used for the simulation model. The vacuum region was 30 Å to avoid artificial interactions between periodic images. During relaxation, the geometric structure was optimized until all the residual forces on each atom were smaller than 0.05 eV/Å. For the geometrical optimization setting, the total energy change and displacement were set to 2.0 × 10⁻⁵ eV and 0.002 Å, respectively [35,36]. An equally spaced k-points mesh of 3 × 3 × 1 was employed to evaluate the electronic state integrations in the Brillouin zone. The adsorption energy (*E_{ads}*) of O₂ and *OOH was calculated by Eq. 9:

$$E_{ads} = E_{system} - E_c - E_x \quad (9)$$

where *E_{system}* is the total energy of heteroatom-doped carbon for O₂ or *OOH adsorption, *E_c* is the energy of heteroatom-doped carbon, and *E_x* is the energy of O₂ or *OOH.

3. Results and discussion

3.1. Structural and compositional characterization

The synthetic process for heteroatoms-doped (N,P and N,S) HMCS catalysts is schematically illustrated in Fig. 1a. Firstly, a spherical silica (SiO₂) template with an average particle size of ~200 nm (Fig. S1a) was prepared by the Stöber method [1]. Then, the SiO₂ nanospheres were mixed with dopamine (DA) monomer to react overnight at 40 °C, and DA was polymerized on the surfaces of SiO₂ nanospheres to form SiO₂ @polydopamine nanospheres with a core-shell structure (SiO₂ @PDA) (Fig. S1b). After PDA coating, the surface of SiO₂ nanospheres became rough. Next, SiO₂ @PDA was transformed into N,C-SiO₂ after pyrolysis at 900 °C in Ar to remove components containing H and O (Fig. S2). Furthermore, the SiO₂ template was etched with NaOH to form N-doped hollow mesoporous carbon nanospheres (N-HMCS) (Fig. S3). Finally, P and S species were introduced by high-temperature phosphorization and sulfurization to obtain N,P- and N,S-codoped hollow mesoporous carbon nanospheres (N,P-HMCS and N,S-HMCS). The morphology and structure of synthesized N-HMCS, N,P-HMCS, and N,S-HMCS were characterized by means of scanning electron microscopy (SEM) and transmission electron microscopy (TEM). From Fig. S3a-b, Fig. 1b-c, and Fig. 1f-g, it can be concluded that the carbon materials possess typical nanospherical morphology with smooth surfaces and uniform core space, which did not change significantly after P or S doping. In addition, the high-resolution TEM (HRTEM) images of N,P-HMCS and N,S-HMCS, shown in Fig. 1d and Fig. 1h, reveal that the shell thickness of the hollow nanospheres is as thin as ~50 nm. Especially, there are some mesopores in the shells of the nanospheres, which may have originated from the decomposition of PDA and the reaction involving P- or S-containing

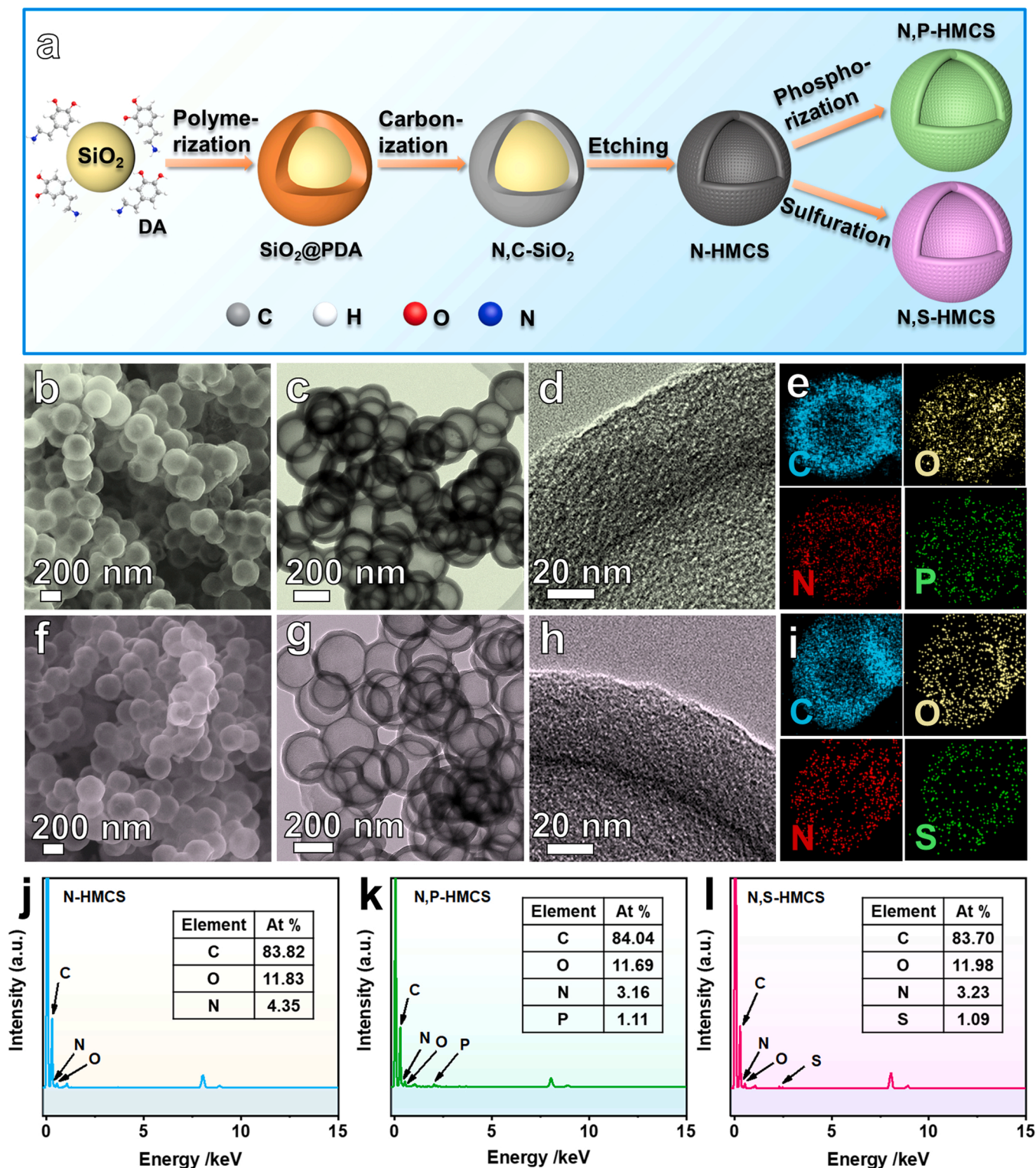


Fig. 1. (a) The schematic representation of synthetic process for N,P-HMCS and N,S-HMCS. (b) SEM image, (c-d) TEM and HRTEM images, and (e) EDS elemental mapping images of N,P-HMCS. (f) SEM image, (g-h) TEM and HRTEM images, and (i) EDS elemental mapping images of N,S-HMCS. EDS spectra of (j) N-HMCS, (k) N,P-HMCS, and (l) N,S-HMCS.

substances during the pyrolysis process (the diffusion and release of the formed gas). These results signify that high-temperature phosphorization and sulfuration do not change the hollow structure of N-HMCS. It can also be seen from the corresponding high-resolution SEM images in Fig. S4 that the spherical structure remains intact despite high-temperature treatment, illustrating the superior thermal stability of

the hollow structure. According to the previous report, the hollow structure can be beneficial to the mass transfer during the oxygen reduction process on the basis of the increased specific surface area and exposure of active sites [37]. Moreover, no obvious lattice fringes are observed from the surface of the shell in HRTEM image, manifesting no complete graphitization of N,P-HMCS and N,S-HMCS [38]. Their

high-angle annular dark field scanning TEM (HAADF-STEM) images in Fig. S5a-b and the corresponding energy-dispersive spectroscopy (EDS) elemental mapping images of N,P-HMCS and N,S-HMCS, shown in Fig. 1e and Fig. 1i, manifest the homogeneous distribution of C, N, O, P, and S in a series of hollow nanospheres. Moreover, from the relevant EDS data of the synthesized catalysts in Fig. 1j-l, the estimated nitrogen content is about 4.35, 3.16, and 3.23 at% for N-HMCS, N,P-HMCS, and N,S-HMCS, respectively. The contents of P and S are 1.11 at% and 1.09 at%, respectively. Clearly, the secondary doping resulted in the decrease of N content presumably due to the partial substitution of N atoms by P or S atoms, forming new active sites and regulating the electronic structure.

The physicochemical characteristics of the synthesized samples were investigated by means of X-ray diffraction (XRD), Raman spectroscopy, and X-ray photoelectron spectroscopy (XPS). Fig. 2a shows the Raman spectra of N-HMCS, N,P-HMCS, and N,S-HMCS catalysts, and all samples have well-defined *D* and *G* bands. The *D* band at 1352 cm^{-1} is belonged to the vibration of disordered graphitic carbon atom. And the *G* band at 1590 cm^{-1} is caused by the symmetric vibration of sp^2 carbon atom in a graphitic layer, which further proves that the HMCS contains graphitic carbon components [14,39]. The intensity ratio of the *D* band to the *G* band (I_D/I_G) has an obvious increase when the second P or S dopant with a larger atomic radius are introduced: 1.62 for N-HMCS < 1.97 for N,P-HMCS < 2.31 for N,S-HMCS. This suggests that N,P- and N,S-codoping effect increases the degree of carbon atom lattice defects. An apparent reason may be the presence of some small molecules in the form of gas released during high-temperature reactions [40,41]. Additionally, the different electronegativity of P, S, and N can contribute to some extent. Specifically, S and N belong to diagonal elements and have similar chemical properties, which lead to the rearrangement of carbon charges under the action of intense electron absorption and result in a stronger distortion of the carbon lattice at high temperature [6,21]. In the XRD patterns of N-HMCS, N,P-HMCS, and N,S-HMCS (Fig. 2b), broad reflections with low intensity are observed at $2\theta = 23^\circ$ and 44° , which are assignable to (002) and (101) crystallographic planes of graphitic carbon [38,42]. The XRD results are consistent with the HRTEM data, indicating no obvious change in the graphitic phase after P or S doping.

In addition, XPS can provide information on the surface elemental composition, content, chemical bonding state, etc. of the heteroatom-doped carbon materials [43]. As displayed in Fig. 2c, XPS spectra manifest that C, N, O, and P (or S) elements are consist in the corresponding heteroatom-doped HMCS. The XPS and EDS data shown in Table S1 are consistent. From the XPS results, the proportion of N is approximately 4.1% for N-HMCS, which is reduced to 3.5% for N,P-HMCS and 3.5% for N,S-HMCS after phosphorization and sulphurization. Fig. 2d-h shows the corresponding high-resolution XPS spectra of C 1s, N 1s, O 1s, P 2p, and S 2p of the prepared catalysts. In Fig. 2d, the high-resolution C 1s XPS spectrum of N-HMCS, N,P-HMCS, and N,S-HMCS can be deconvoluted into four peaks centered at 284.5, 285.4, 286.5, and 288.2 eV, which correspond to the C-C/C=C, C-N/C=N (C-P; C-S), C-N/C-O and O-C=O bonds, respectively [24,44,45]. The C-N/C=N peaks at 285.4 eV for all samples confirm the successful doping of N atoms into the carbon framework. In Fig. 2e, high-resolution N 1s spectra of N-HMCS, N,P-HMCS, and N,S-HMCS can be divided into four types: pyridinic N (398.3 eV), pyrrolic N (400.2 eV), graphitic N (401.2 eV), and N-oxide (402.8 eV), which are typically observed in N-doped carbon [46]. The ratios of the different deconvoluted C 1s and N 1s bonding types are summarized in Tables S2 and S3. For N-HMCS, the total composition of C-C/C=C, C-N/C=N, C-O, and O-C=O is approximately 63.26%, 16.46%, 5.91%, and 14.37%, respectively. However, after introducing the P atoms, the C-N/C=N/C-P proportion increased to 20.01%, while the O-C=O proportion decreased to 10.74% with the change of elemental composition ratio. Similarly, the C-N/C=N/C-S proportion increased to 21.09% and the O-C=O proportion decreased to 10.29% after N,S codoping. Notably, pyrrolic N dominates the N configuration in

N-HMCS, while graphitic N is the major type (54.28%) in N,P-HMCS and pyridinic N takes a larger part of N forms (38.99%) in N,S-HMCS (Fig. 2i). The three N configurations and their electronic constructions with adjacent carbon are schematically represented in Fig. 2j. We speculate that the introduction of P and S can further expand the charge delocalization of carbon and affect the formation of N configuration. The continuous high-temperature environment triggers the transformation of unstable pyrrolic N to graphitic N configuration [47,48]. Therefore, graphitic N exists as the dominant species in the systems. On the other hand, sulfurization may also form more defect and edge sites of carbon atoms on the graphitic surface, increasing the pyridinic N configuration of edge sites [6,49]. These results sufficiently demonstrate that introducing the P and S species can regulate the content and bonding types of N, which may affect the ORR activity and selectivity. Fig. 2f shows the high-resolution O 1s XPS spectra of N-HMCS, N,P-HMCS, and N,S-HMCS, which can be divided into three typical peaks: O=C-C (530.2 eV), O-C=O (531.2 eV), and C-O (532.7 eV) [50,51]. The proportion (%) of these bonding types is given in Table S4. The content of O-C=O decreases with the P or S doping, coinciding with the change in the composition of O-C=O of the C 1s for each sample. The high-resolution P 2p XPS spectrum in Fig. 2g reveals two peaks at 131.9 eV and 134.0 eV, which correspond to C-P and O-P, respectively, and the content of the C-P bond reaches 81.65% (Table S5). This confirms that the P atoms were favorably doped into the N-doped carbon framework [52]. Correspondingly, the high-resolution S 2p XPS spectra in Fig. 2h can be deconvoluted into five peaks. The two peaks at 164.1 eV and 165.2 eV are assigned to the C-S-C and S=C bonds, belonging to thiophane-S groups, and account for 65.35% of S bond types (Table S6), which is closely related to ORR activity [24,53]. Besides, the peaks at 167.3, 168.1, and 169.4 eV can be ascribed to S-oxide groups (C-SO_x-C, $x = 2, 3, 4$) [54]. Thus, the S atom was also successfully doped into the N-doped carbon framework. According to the previous reports [52,55,56], both graphitic N and pyridinic N play a key role in catalyzing the ORR. In this work, graphitic N is relatively increased after P is introduced into N-HMCS, and pyridinic N is relatively increased after S is introduced into N-HMCS. Therefore, it is thought that they may affect the catalytic activity and the reaction pathway toward ORR along with the formed C-P and C-S bond.

The specific surface areas and pore structures of the synthesized catalysts were characterized by N₂ adsorption-desorption measurements. As shown in Fig. 3a-c, type IV adsorption-desorption isotherms are observed for N-HMCS, N,P-HMCS, and N,S-HMCS, indicating the coexistence of micropores and mesopores. The doping of P or S causes an increase in the BET specific surface area and pore volume (Fig. 3a-c), whereas the pore size increases from 2–5 nm for N-HMCS to 2–10 nm for N,P-HMCS and N,S-HMCS. The enlargement of the pore structures is attributed to the release of P- and S-containing gases during the high-temperature process. Such features of N,P-HMCS and N,S-HMCS are beneficial for improving the permeability of gas and liquid and increasing the mass transfer efficiency for the ORR process [57].

In addition, the work function can support in understanding the relation between the electronic properties induced by defect engineering and heteroatom doping with the ORR electrocatalytic activity and selectivity. It shows the minimum energy required for electrons to move from the Fermi level to the vacuum level, which means that the lower the work function of catalysts, the easier the electron transfer for ORR [50]. In order to further explore the electronic modulation mechanism of P or S atoms in N-HMCS, the work function and related information of the catalysts were obtained by ultraviolet photoemission spectroscopy (UPS) [58,59]. In Fig. 4a-c, the cutoff level (E_{cutoff}) and the valence band maximum (E_v) were confirmed, and the work function (Φ) can be calculated by Eq. 9:

$$\Phi = h\nu(21.22\text{ eV}) - |E_f| - E_{\text{cutoff}} \quad (9)$$

Fig. 4d shows the energy band structures of the synthesized catalysts.

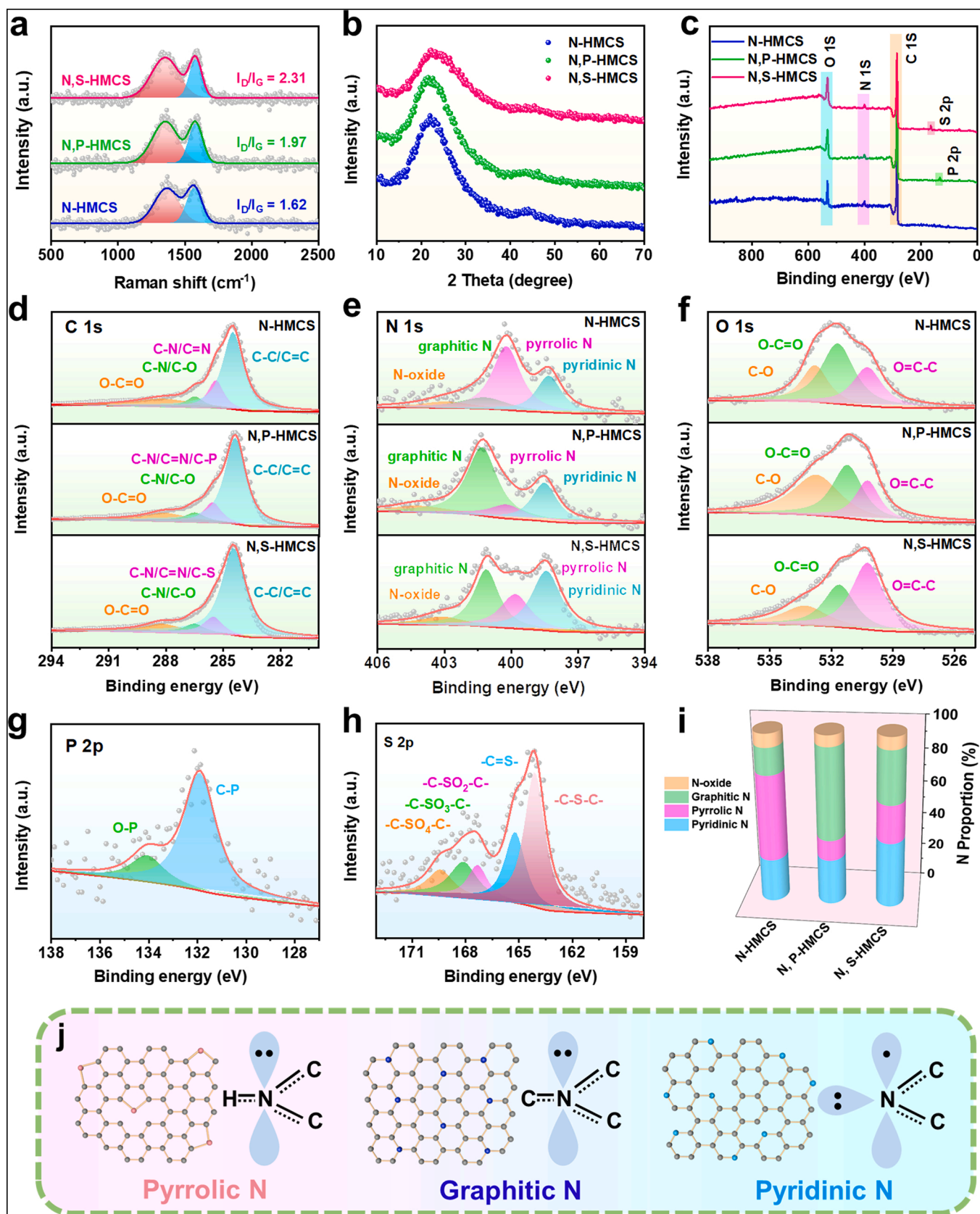


Fig. 2. (a) Raman spectra, (b) XRD patterns, (c) XPS spectra, and deconvoluted high-resolution XPS spectra of (d) C 1s, (e) N 1s, and (f) O 1s for N-HMCS, N,P-HMCS, and N,S-HMCS. (g) High-resolution P 2p spectra of N,P-HMCS, (h) high-resolution S 2p spectra of N,S-HMCS, (i) proportion (%) of N 1s bonding types, and (j) schematic diagram of the N configuration incorporated into the synthesized catalysts.

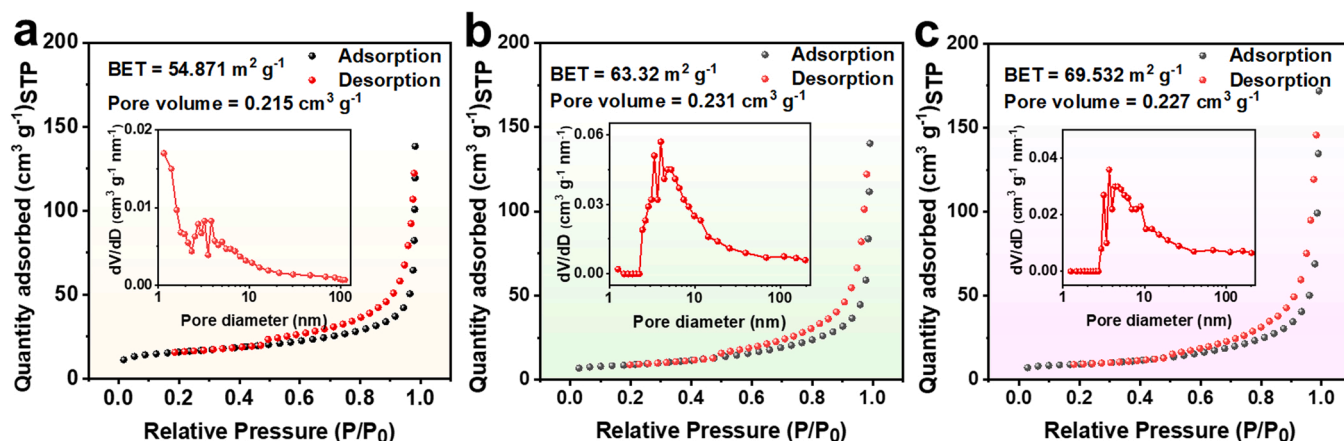


Fig. 3. N_2 adsorption-desorption isotherms and pore-size distribution curves (insets) of (a) N-HMCS, (b) N,P-HMCS, and (c) N,S-HMCS.

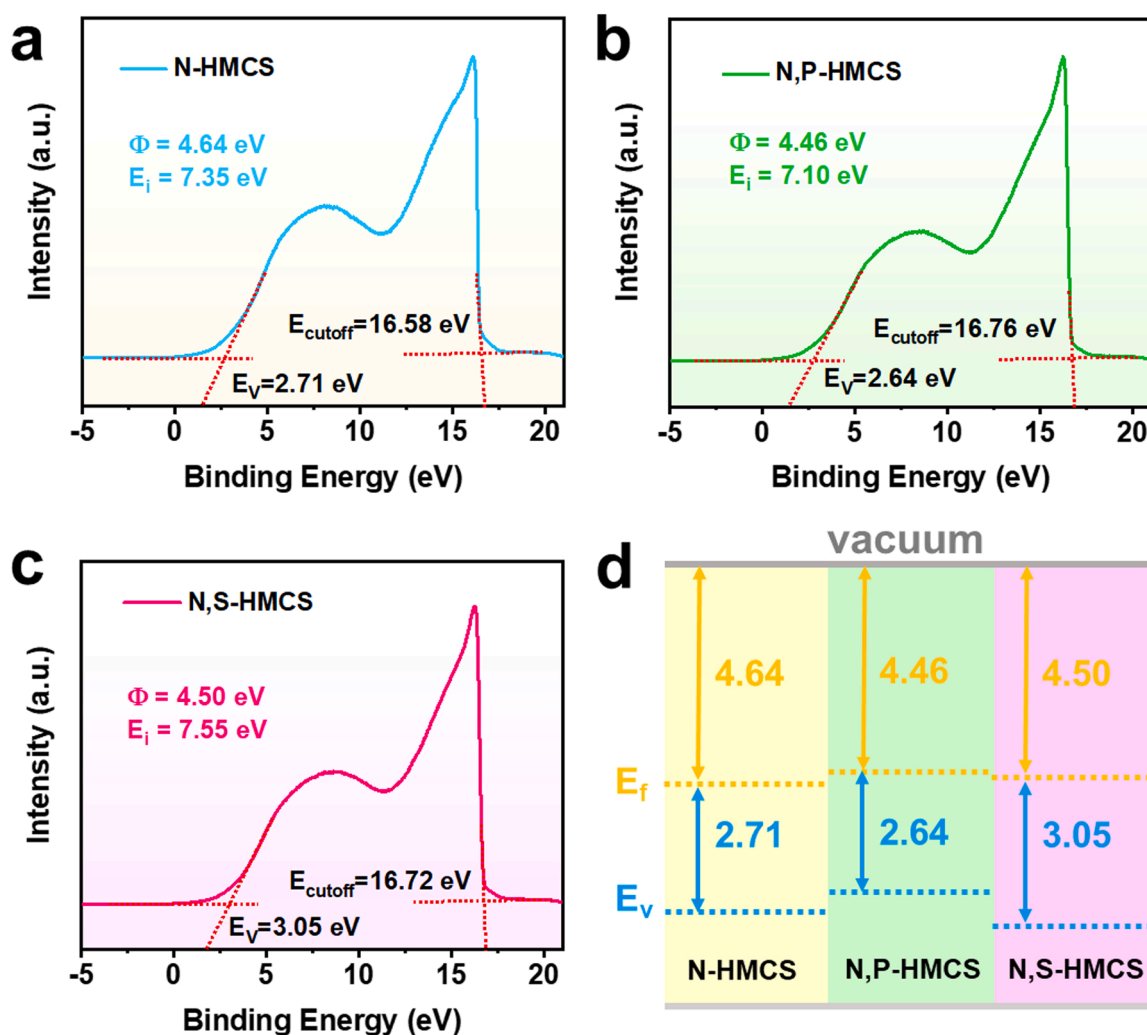


Fig. 4. UPS spectra of (a) N-HMCS, (b) N,P-HMCS, and (c) N,S-HMCS and (d) energy band structures of the synthesized catalysts obtained from UPS analysis.

The work functions of the synthesized catalysts decreases in the following order: N-HMCS (4.64 eV) > N,S-HMCS (4.50 eV) > N,P-HMCS (4.46 eV), indicating that the P or S doping can improve the electron transfer efficiency of N-HMCS and activate the reaction thermodynamics. The N,P-HMCS possesses the smallest work function, signifying the outstanding conductivity. Besides, the ionization potential can provide information about the ability of the catalyst to donate or

accept electrons, which can be obtained by Eq. 10:

$$E_i = \Phi + E_v \quad (10)$$

The N,P-HMCS has the lower ionization potential (7.10 eV) compared to N-HMCS (7.35 eV), implying that it is inclined to provide an electron-rich environment in term of the C-P bond with less electronegativity of P atoms. Meantime, the C-S bond formed by doping of

highly electronegative S atoms leads to an electron-deficient environment, corresponding to the higher ionization potential of N,S-HMCS (7.55 eV). As mentioned above, the N atoms possess a higher electronegativity than the C atoms and are more inclined to attract electrons from C. As a result, this breaks the electrical neutrality of sp^2 graphene carbon in the carbon material and makes C near the N dopant to a partially positive charge. The introduction of P and S atoms breaks the charge balance established by N doping. The P atoms tend to donate electrons to C, while the S atoms prefer to receive electrons from C, implying that the charge of C adjacent to the dopant is redistributed to a new equilibrium state. It has been reported that whether the dopant is electron-rich or electron-deficient, it causes C to have partially positive or negative charge. Thus, it leads to changes in atomic charge and spin density and further forming the key active sites conducive to the interaction and adsorption of carbon-based materials with O_2 and related intermediates [40,54,60]. Therefore, it is expected that these two different electronic environments for N,P-HMCS and N,S-HMCS could affect the adsorption energy of oxygen-containing intermediates, influencing the ORR activity and leading to different ORR pathways.

3.2. ORR performance and its mechanism

Before the ORR activity tests, the electrochemical active surface areas (ECSA) of all catalysts were estimated according to the electrochemical double-layer capacitance (C_{dl}) (Figs. S6–8) measured by cyclic voltammetry (CV) in N_2 -saturated 0.1 M KOH electrolyte with different scan rates ($10\text{--}60\text{ mV s}^{-1}$) at $0.95\text{--}1.05\text{ V}$ vs. RHE. The C_{dl} values decrease in the following order: 9.72 mF cm^{-2} for N,P-HMCS $> 9.45\text{ mF cm}^{-2}$ for N,S-HMCS $> 3.25\text{ mF cm}^{-2}$ for N-HMCS, suggesting that N,P-HMCS and N,S-HMCS have greater ECSAs and may provide more reactive sites for the ORR process. The CV curves of N-HMCS, N,P-HMCS, and N,S-HMCS on rotating disk electrode (RDE) at 1600 rpm in 0.1 M KOH electrolyte saturated with N_2 and O_2 are shown in Fig. 5a. The similar profiles of the three samples indicate that the hollow carbon nanospheres are structurally stable after heteroatom doping. Fig. 5b shows the complete ORR response of these catalysts in oxygen, avoiding the overestimation of the dynamic current due to the contribution of the capacitance background. In addition, the onset potential (E_{on}) and half-wave potential ($E_{1/2}$) of electrocatalysts are reliable criteria to assess ORR activity. The higher E_{on} and $E_{1/2}$ values indicate the higher ORR activity. It is clear that the ORR activity was improved after the introduction of P and S atoms according to E_{on} and $E_{1/2}$ values of N,P-HMCS (0.90 V, 0.77 V) $>$ N,S-HMCS (0.89 V, 0.75 V) $>$ N-HMCS (0.87 V, 0.72 V) [61]. The slight difference in the E_{on} and $E_{1/2}$ values for N,

P-HMCS and N,S-HMCS stems from the different degree of charge rearrangement caused by the formation of C–P and C–S bonds. Change in the E_{on} and $E_{1/2}$ values of the synthesized catalysts is also consistent with that of ECSA. It is worth noting that N,P-HMCS shows a well-defined diffusion limited current from 0.70 V, which is close to the theoretical thermodynamic potential ($\sim 0.7\text{ V}$) of the ORR via the two-electron pathway, confirming its outstanding selectivity for ORR [62,63].

The ORR activity and selectivity of electrocatalysts are essential for the electrochemical reduction of oxygen to H_2O_2 or H_2O . The closer the electron transfer number (n) is to 2 in the ORR process, the higher selectivity for H_2O_2 , and the two-electron process is dominant. Conversely, the closer the n is to 4, the higher selectivity for H_2O , and the four-electron process proceeds mainly [5,63,64]. These parameters of the three different heteroatom-doped hollow carbon nanomaterials were estimated in an O_2 -saturated 0.1 M KOH solution via LSV measurements using the rotating ring-disk electrode (RRDE) technique with 1600 rpm. All electrochemical results of N-HMCS, N,P-HMCS, and N,S-HMCS exhibit a response under N_2 (Fig. S9). Fig. 6a shows the oxygen reduction current (I_d) detected on the disk electrode at $0\text{--}1.1\text{ V}$ vs. RHE and the oxidation current (I_r) of H_2O_2 detected on the ring electrode at 1.2 V vs. RHE. The limiting current densities (j_L) of N-HMCS, N,P-HMCS, N,S-HMCS, and commercial 20 wt% Pt/C catalysts are 1.76, 2.16, 3.21, and 5.61 mA cm^{-2} at 0.2 V vs. RHE, respectively.

Larger j_L values were obtained for the codoped samples, particularly for N,S-HMCS, which can be ascribed to the increase of graphitic N in the system resulted from the secondary P or S doping [61,65]. However, it is still unclear why the N,P-HMCS with a higher graphitic N content did not have a stronger current output than the N,S-HMCS. A deeper insight into the effect of second heteroatom codoping is needed. The C–P bond formed by doping of P with a larger atomic radius may distort the graphene sp^2 lattice, seriously damage the spin density of C, cause the deviation from the plane, and generate massive deformation, which are detrimental to the ORR activity [66]. Meantime, the C–S covalent bond of N,S-HMCS induces larger asymmetrical spin and higher charge density on the carbon surface, enhancing the ORR activity to a greater extent [67]. In addition, there is a significant difference in I_r after heteroatomic doping. Compared to that of N-HMCS, the I_r value of N,P-HMCS increases, while the I_r value of N,S-HMCS decreases. This implies that the introduction of P increases the generation of H_2O_2 , while the introduction of S inhibits the generation of H_2O_2 .

As exhibited in Fig. 6b, the n values of N-HMCS, N,P-HMCS, and N,S-HMCS are about 3.15, 2.22, and 3.72 at a wide range of potential ($0\text{--}0.8\text{ V}$) for ORR. Fig. 6c shows the corresponding selectivity of H_2O_2

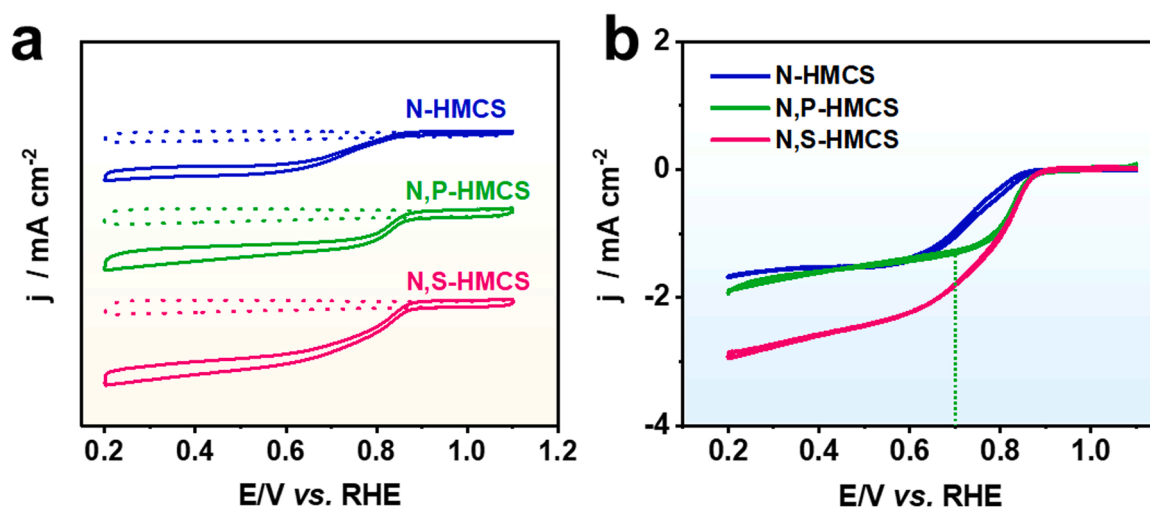


Fig. 5. (a) Cyclic voltammetry (CV) curves of N-HMCS, N,P-HMCS, and N,S-HMCS in 0.1 M KOH electrolyte saturated with N_2 (dotted line) and O_2 (solid line) with 1600 rpm at 5 mV s^{-1} scan rate and (b) cathodic and anodic scan profiles after subtraction of capacitive currents based on (a).

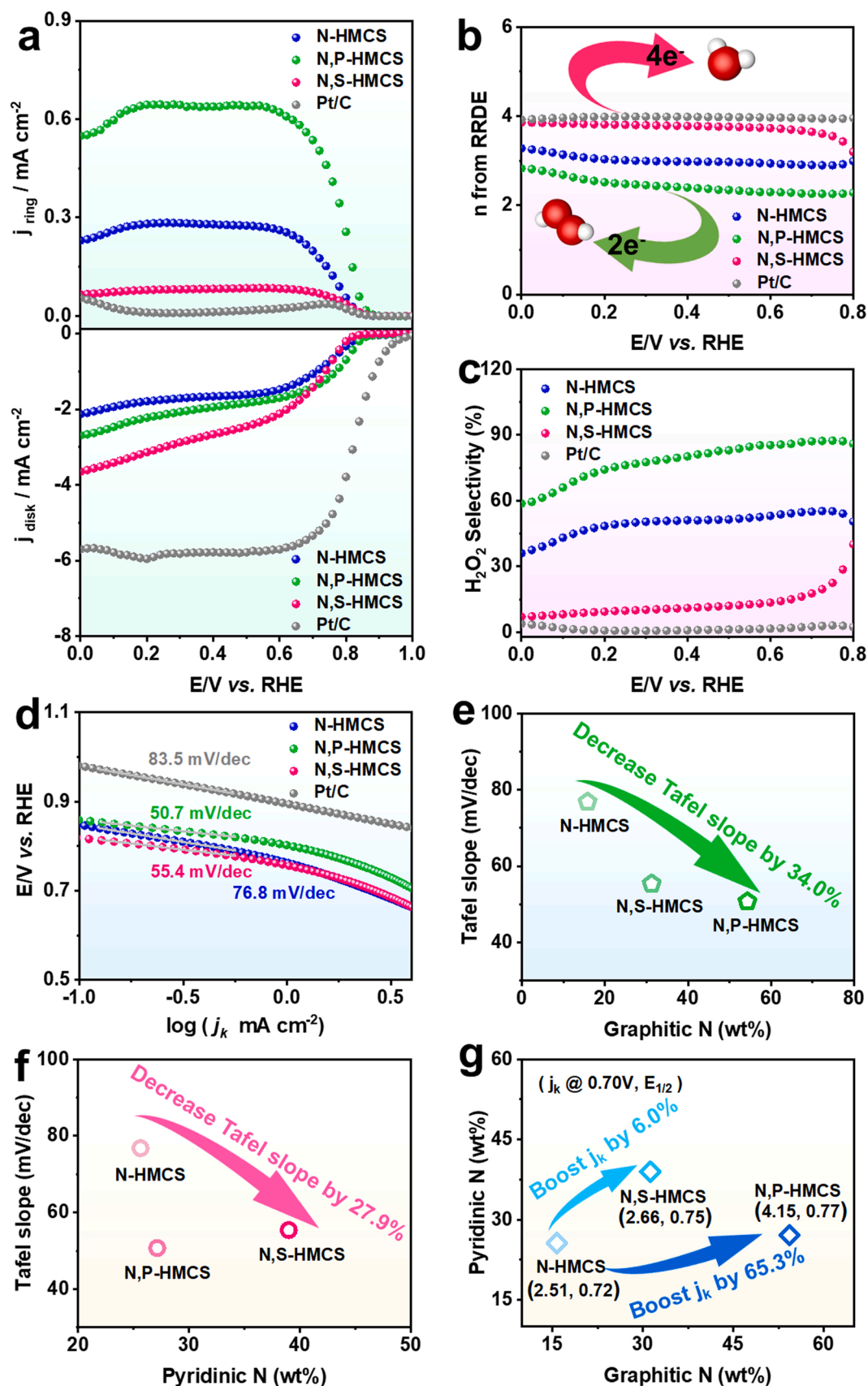


Fig. 6. (a) LSV curves of N-HMCS, N,P-HMCS, N,S-HMCS, and commercial Pt/C catalyst obtained using RRDE measurement with a rotation rate of 1600 rpm in O_2 -saturated 0.1 M KOH, (b) electron-transfer number, (c) H_2O_2 selectivity, and (d) corresponding Tafel plots. (e) Relation between Tafel slope and graphitic N proportion, (f) relation between Tafel slope and pyridinic N proportion, and (g) relationship between ORR activities ($j_k @ 0.70\text{ V}$ and $E_{1/2}$) and N (pyridinic N and graphitic N) proportion.

electro-generation at various potentials. Thus, the ORR of N-HMCS follows a mixed two-electron/four-electron transfer mechanisms, while the N,P-codoped HMCS is more inclined to catalyze two-electron ORR, making it a promising electrocatalyst to produce H_2O_2 . In contrast, a close four-electron ORR occurs more easily on the N,S-codoped HMCS. Similarly, the LSV measurements of three samples were conducted under rotating speed from 400 to 1600 rpm with RDE. The n values of N-HMCS, N,P-HMCS, and N,S-HMCS were evaluated using by the Koutecký-Levich (K-L) equation with the potential at 0.2, 0.25, 0.3, 0.35, and 0.4 V and found to be 3.15, 2.22, and 3.72 (Fig. S10–12), respectively, which is consistent with the results of RRDE measurements. It has been reported that the catalytic activity and H_2O_2 selectivity in ORR can be significantly improved by introducing heteroatoms to disrupt the integrity of the π -conjugated system within the carbon framework and change the electronic structure of nanocarbon catalysts [68,69]. N,P and N,S codoping is an attractive strategy to trigger and control the ORR selectivity. Among the three heteroatoms-doped HMCS-based catalysts, a subtle difference in the chemistry of the N-sites can lead to greater changes in the H_2O_2 yields despite their similar morphology, structure, and N/C/O components. After introducing P into N-HMCS, graphitic N significantly increases and plays a key role in catalyzing H_2O_2 generation by a two-electron reaction pathway of ORR. In the case of N,S-HMCS, the S atoms influence the content of pyridinic N, changing as the largest part, which could act as the active site of the four-electron reduction pathway in ORR process. However, the N,P-HMCS with the lowest work function does not increase the activity (limiting diffusion current) significantly, but regulate the selectivity, while the N,S-HMCS with lower work function could increase the activity and control selectivity. From the ionization energy perspective, we attribute this to the fact that N,P-HMCS possesses a smaller E_i value and the N,S-HMCS has a larger E_i compared to N-HMCS. Under the action of less electronegative P atoms, P acts as the donor atom to present an electron-rich state on the surface of the carbon matrix. That weakens the adsorption of oxygen-containing intermediates and promotes the further desorption of $^*\text{OOH}$ before the O–O bond breaks, accelerating the two-electron ORR pathway. Conversely, the S atom with a stronger electron-gaining ability makes the surface of the C substrate electron-lacking, which strengthens the adsorption of $^*\text{OOH}$, thereby promoting the rupture of the O–O bond and carrying out the four-electron ORR pathway.

In addition, to understand the reduction mechanism of the ORR process on heteroatom co-doped HMCS-based catalysts in detail, it is necessary to analyze the correlation of reaction kinetics and N configuration caused by heteroatom doping. The reaction kinetics of ORR was analyzed by Tafel slope, which was calculated by the relation between electrode potential (vs. RHE) and kinetic current density (j_k) (Fig. 6d). The lower Tafel slope means faster reaction kinetics. As shown, N,P-codoped HMCS (50.7 mV/dec) and N,S-codoped HMCS (55.4 mV/dec) possess a smaller Tafel slope than N-HMCS (76.8 mV/dec) and commercial 20.0 wt% Pt/C (83.5 mV/dec). Based on the hypothesis of Damjanovic et al. [70,71], the rate-determining step (RDS) on the Pt electrode or other precious metals is widely considered to be the first electron transfer step to the adsorbed O_2 molecules, regardless of the presence of a rapid proton transfer. The theoretical Tafel slope is equal to $2.303RT/(n + 0.5)F$, that is, when the RDS involves the first proton transfer ($n = 0$), the expected Tafel slope is 119.1 mV/dec [72,73]. The possible reason for the inconsistency between the two results might be the existence of an adsorption layer on the Pt electrode. However, the Tafel slope of the HMCS-based catalyst was between 50 and 80 mV/dec. According to the results of overlapping for cathodic and anodic cyclic scans in CV (Fig. 5b), we could exclude the interference of the adsorbed layer, which indicates that the proton transfer of adsorbed O_2 molecules ($^*\text{O}_2 + \text{H}_2\text{O} + e^- \rightarrow ^*\text{OOH} + \text{OH}^-$) on the HMCS-based catalyst is faster than that of the Pt electrode [19]. As displayed in Fig. 6e, the Tafel slope exhibits a positive correlation with graphitic N, which decreases with the increases of graphitic N content. Compared with N-HMCS, the Tafel slope of N,P-HMCS with the highest graphitic N content decreases by

34.0%. However, such relationship cannot be observed well between pyridinic N with the Tafel slope (Fig. 6f). These results suggest that heteroatom-doped HMCS-based catalysts exhibit different relationships between ORR kinetics and N configuration. Moreover, N,P-HMCS boosts the increase of j_k by 65.3%, while N,S-HMCS boosts the increase of j_k by only 6.0% in comparison to N-HMCS (Fig. 6g).

The four-electron ORR and two-electron ORR pathways are competing. For N-doped carbon-based electrocatalysts, the introduction of N can enhance the activity of ORR, while the selectivity of ORR is in a mixed state in most cases. Theoretically, the two-electron or four-electron ORR pathway may depend on the adsorption of $^*\text{OOH}$ intermediate on the surface of catalysts. A strong adsorption of $^*\text{OOH}$ leads to the rupture of the O–O bond and initiates the four-electron pathway, while a weak adsorption of $^*\text{OOH}$ favors its desorption and promotes the two-electron pathway. In this work, the P and S atoms with larger radii were introduced to the N-doped hollow structure carbon nanospheres, which modifies the electronic structure of the C atoms, realizing the generation of abundant defect sites and the regulation of N content and configuration. In comparison to the S atom, the weaker electronegativity of the P atom may make it an electron-donor in N,P-codoped hollow carbon nanospheres, and the formed C–P bond increases the density of an electron cloud in the delocalized π -conjugated system, which may result in the weak adsorption of $^*\text{OOH}$ and produce H_2O_2 by a facile $^*\text{OOH}$ desorption [21,64]. Moreover, we confirm that both N,S-HMCS and N,P-HMCS have lower work functions, but the N,P-HMCS with low ionization energy also weakens the ability to stabilize $^*\text{OOH}$ intermediates due to the extreme of the graphene sp^2 lattice by doping with P a large radius, thus resulting in two-electron ORR [66]. On the contrary, the S atom as an electron-acceptor reduces the density of an electron cloud of the conjugated system in the C–S bond, thereby leading to a strong adsorption of $^*\text{OOH}$ and promoting the dissociation of $^*\text{OOH}$ to undergo a four-electron ORR [64]. In addition, N,P co-doping increases the graphitic N content, while N,S co-doping increases the pyridinic N content. This may also be another decisive factor affecting the ORR selectivity. Thus, based on the mentioned results, we propose the possible mechanism of two-electron and four-electron pathways of ORR induced by N,P- and N,S-codoped HMCS electrocatalysts (Fig. 7). The rich graphitic N site can act as a donor to provide an electron to the delocalized conjugated system to cause charge redistribution, thereby enhancing the oxygen adsorption on the adjacent C atoms of graphitic N [14]. Subsequently, the adsorbed oxygen molecules couple with nearby proton to form $^*\text{OOH}$, and eventually, this unstable structure tends to balance its charge, so that to release the anchored $^*\text{OOH}$ from the graphitic N site for H_2O_2 generation [18]. When the catalyst is rich in pyridinic N at the edge site, ORR can continue from the two-electron pathway to the four-electron pathway, forming H_2O , because this loss of unbalanced charge cannot drive the release of the anchoring $^*\text{OOH}$ intermediate [14,16,18]. Above all, this work elucidates the ORR selectivity by altering the electronic structure by N,P- or N,S-codoping. The two-electron pathway relies on the synergistic catalysis of the less electronegative C–P bond and the graphitic N site, while the four-electron pathway depends on the synergistic catalysis of the more electronegative C–S bond and the pyridinic N site. Therefore, the ORR pathway can be manipulated by regulating the electronic structure of the system with the doping of different heteroatoms to enhance/weaken the binding energy to $^*\text{OOH}$.

To further confirm the above-given conjecture for the different ORR behaviors observed for three heteroatoms-doped HMCS-based materials, we conducted a study on a thorough-paced mechanism by first-principles calculations. In general, the ORR proceeds in alkaline media according to the following steps [74,75]:

Four-electron ORR: Step 1: $^*\text{O}_2 + \text{H}_2\text{O} + e^- \rightarrow ^*\text{OOH} + \text{OH}^-$

Step 2: $^*\text{OOH} + e^- \rightarrow ^*\text{O} + \text{OH}^-$

Step 3: $^*\text{O} + \text{H}_2\text{O} + e^- \rightarrow ^*\text{OH} + \text{OH}^-$

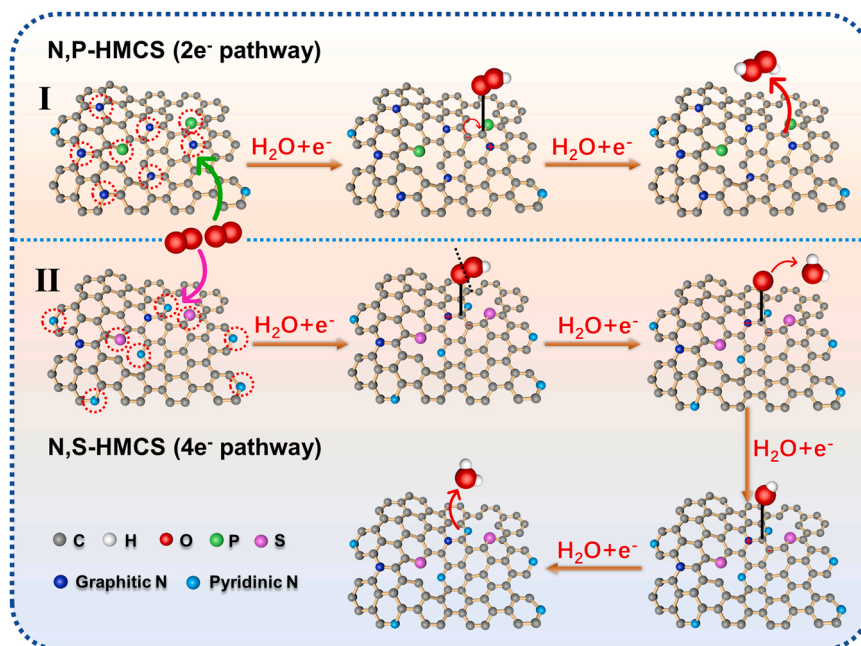


Fig. 7. Possible mechanism for the two-electron and four-electron ORR pathways for N,P-HMCS and N,S-HMCS.

Step 4: $^*\text{OH} + \text{e}^- \rightarrow \text{OH}^- + ^*$

Two-electron ORR: Step 1: $^*\text{O}_2 + \text{H}_2\text{O} + \text{e}^- \rightarrow ^*\text{OOH} + \text{OH}^-$

Step 2: $^*\text{OOH} + \text{e}^- \rightarrow \text{OOH}^-$

It is known that the key to achieving high ORR activity is the effective adsorption of O_2 molecules on the catalyst surface, while the selectivity of four-electron and two-electron ORR is mainly determined by two competing reactions of $^*\text{OOH}$ on the catalyst surface ($^*\text{OOH} + \text{e}^- \rightarrow ^*\text{O} + \text{OH}^-$ and $^*\text{OOH} + \text{e}^- \rightarrow \text{OOH}^-$) [36,64]. For the four-electron

pathway, the O-O bonds in $^*\text{OOH}$ intermediate must be cleaved, requiring the catalyst with strong $^*\text{OOH}$ binding energy. For the two-electron pathway, the O-O bonds in $^*\text{OOH}$ must be retained and make the catalytic material selective to H_2O_2 , requiring the catalyst to possess weak $^*\text{OOH}$ binding energy [76]. Through theoretical analysis, we elucidated the effect of heteroatom doping on ORR activity and selectivity. The configurations of the adsorption sites are constrained to the C position near the doping atoms [18,23,36], as shown in Fig. S13-S15. The adsorption energies of O_2 and $^*\text{OOH}$ for these optimized different models, such as graphitic N, pyridinic N, pyrrolic N, C-P, C-S, graphitic N/C-P, and pyridinic N/C-S, were calculated and the

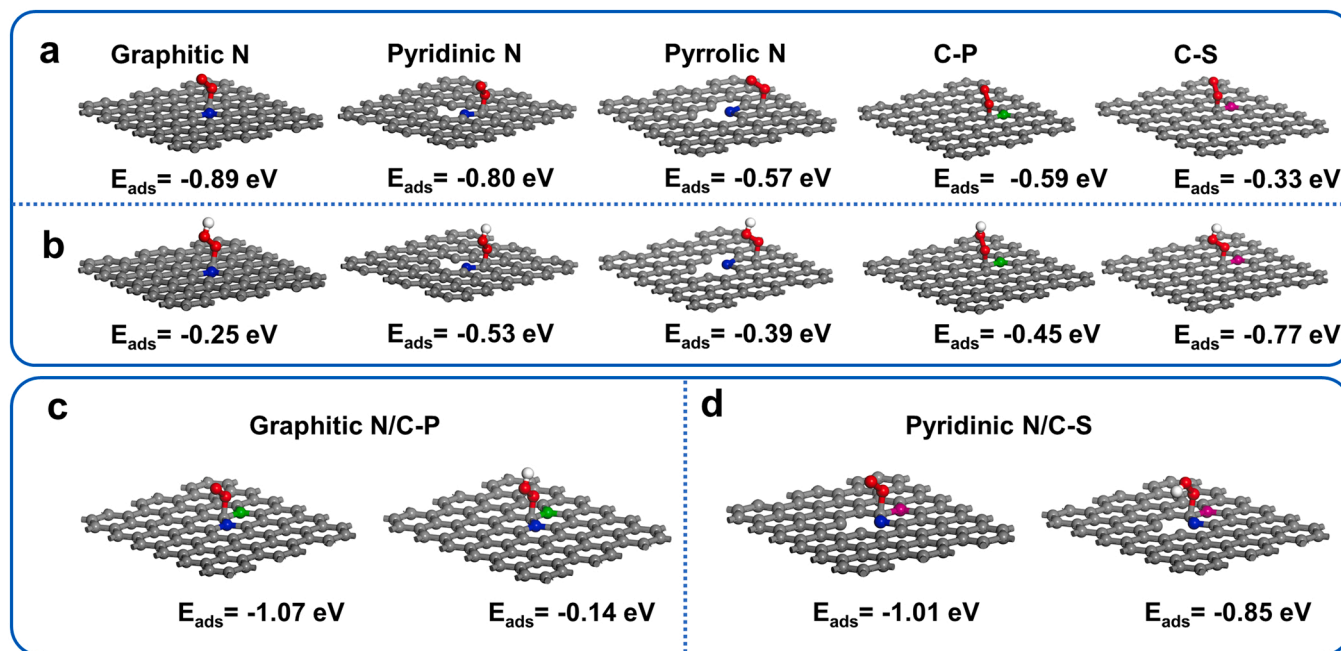


Fig. 8. Optimized different configurations and adsorption energies for O_2 molecule (a) and $^*\text{OOH}$ intermediate (b). The optimized configurations and adsorption energies for O_2 molecule and $^*\text{OOH}$ intermediate on the models of graphitic N/C-P (c) and pyridinic N/C-S (d). The C, N, O, H, P, and S atoms are represented by gray, blue, red, white, green, and purple spheres, respectively.

results are shown in Fig. 8. As shown in Fig. 8a, graphitic N (−0.89 eV) and pyridinic N (−0.80 eV) possess higher adsorption energy for O₂ than pyrrolic N (−0.57 eV), C-P (−0.59 eV), and C-S (−0.33 eV), implying that the rich graphitic N and pyridinic N in the catalyst are the key factors to effectively enhance ORR activity. In addition, by adjusting the electronic structure of the catalyst to enhance or weaken its binding energy with oxygen-containing species, the four-electron and two-electron ORR pathways can be regulated. In these models (Fig. 8b), graphitic N, pyridinic N, and pyrrolic N show the adsorption energies of −0.25 eV, −0.53 eV, and −0.39 eV for *OOH, respectively. Besides, the C-P bond possesses smaller *OOH adsorption energy (−0.45 eV) when *OOH is attached to the near C atoms, suggesting that the presence of the C-P bond responds positively to the selectivity of H₂O₂ via a two-electron pathway. However, the C-S bond near the C atoms shows higher adsorption energy (−0.77 eV) for *OOH, which is conducive to the O-O bond cleavage, and also more conducive to the *O adsorption, significantly improving the four-electron pathway to generate H₂O. This also confirms our conjecture that the two atoms (P and S) with a large difference in their electronegativity can activate adjacent carbon sites, resulting in different adsorption capacities for *OOH. Among them, highly electronegative S atoms strongly attract and hinder *OOH desorption in N,S-HMCS, leading to the four-electron characteristics towards ORR, while less electronegative P atoms weaken the *OOH adsorption in favor of H₂O₂ production, exhibiting two-electron characteristics. We also constructed graphitic N/C-P and pyridinic N/C-S models corresponding to N,P-HMCS and N,S-HMCS catalysts (Figs. 8c and 8d) to further evaluate their adsorption of O₂ and *OOH in the same system. The adsorption energies of graphitic N/C-P for O₂ and *OOH are −1.07 eV and −0.14 eV, respectively, while the adsorption energies of pyridinic N/C-S for O₂ and *OOH are −1.01 eV and −0.85 eV, respectively. These results show that both of them enhance the adsorption of O₂, and graphitic N/C-P possesses the lowest adsorption energy for *OOH, while pyridinic N/C-S has the highest adsorption energy. This further confirms that graphitic N and pyridinic N species play an important role in enhancing the ORR activity, and P and S doping can significantly regulate the ORR selectivity. The obtained results are also consistent with the results from RDE and RRDE experiments.

Apart from the ORR activity and selectivity, methanol tolerance and long-term durability are vital descriptors to reflect the ORR performance. The methanol tolerance of N,P-HMCS, N,S-HMCS, and commercial Pt/C catalysts was investigated (Fig. S16). When 3 M methanol was introduced into 0.1 M KOH electrolyte at 200 s, no remarkable current variations were observed for N,P-HMCS and N,S-HMCS. However, a sharp decrease in the current density for commercial Pt/C was noted, implying that the robust hollow carbon sphere structures of N,P-HMCS and N,S-HMCS have excellent tolerance to methanol poisoning. Besides, a long-term durability of N,S-HMCS (Fig. S17) and N,P-HMCS (Fig. S18) electrocatalysts was evaluated through the chronoamperometric responses using RRDE, where the disk potential was applied at 0.65 V vs. RHE and the ring potential was kept at 1.2 V vs. RHE in O₂-saturated 0.1 M KOH solution. It can be clearly seen that the *I*_r and *I*_d of N,S-HMCS and N,P-HMCS retain more than 95% of the initial current density after 5 h. Moreover, the *n* values of N,S-HMCS and N,P-HMCS remains at 3.88 and 2.20, respectively, and the H₂O₂ selectivity of both samples only changes by 1%, confirming their superior ORR stability.

In addition, the N,P/N,S co-doped catalysts also demonstrate higher stability than commercial Pt/C (Fig. S19). After performing the I-t tests for 5 h, the current retention rates of N,P-HMCS and N,S-HMCS were 98.9% and 96.2%, respectively, which are significantly higher than that of commercial Pt/C (78.1%). In order to further explore the chemical and mechanical stability of catalysts, the morphologies and compositions of N,P-HMCS and N,S-HMCS catalysts after ORR stability tests were characterized by SEM and XPS (Fig. S20 and S21). The SEM image showed that the structure of hollow carbon spheres was still retained

even after ORR tests. In the XPS spectra, it was found that the composition and the content of each element after ORR tests were consistent with those before ORR tests. This confirms the excellent compositional and mechanical stability of the developed catalysts.

3.3. Faradaic efficiency for H₂O₂ production

Besides, the faradaic efficiency (FE) is an indispensable indicator to assess the feasibility of catalysts for practical H₂O₂ electroproduction applications. It also means the catalyst must be stable enough to operate in the electrolyte for a long time to generate a certain amount of H₂O₂. In Fig. 9a, the N,P-HMCS-loaded working electrode (WE) and counter electrode (CE) were separated by a Nafion membrane in an O₂-saturated 0.1 M KOH solution using an H-cell electrolyzer to prevent H₂O₂ crossover. Subsequently, H₂O₂ produced via ORR after 1 h chronoamperometric measurement at the special potential (0.50 V, 0.55 V, 0.60 V, 0.65 V and 0.7 V) can be quantified by Ce(SO₄)₂ solution titration and UV-Visible absorbance, and the detailed calibration system is shown in Fig. S22. As shown in Fig. 9b, the molarity of H₂O₂ produced reached a maximum of 0.6 mM at 0.65 V. Meanwhile, the FE of H₂O₂ maintained above 70% in the potential range of 0.50–0.70 V and reached a maximum value of 82.8% at 0.65 V in 0.1 M KOH solution (Fig. 9c). This stable H₂O₂ yield further highlights the importance of maintaining the graphitic N structure and regulating the active sites of carbon fixation by the C-P bond.

4. Conclusion

In this work, the relation between the N configuration and ORR performance of catalysts after N,P or N,S co-doping in alkaline systems was systematically elucidated. The electrode materials dominated by pyridinic N (N,S-HMCS) or graphitic N (N,P-HMCS) exhibited favorable ORR activity, kinetics, durability, and well-defined selectivity. The outstanding ORR selectivity can be achieved over a wide range of potentials (0–0.8 V) in 0.1 M KOH. Compared to that of N-HMCS, the ORR electron transfer number (*n*) of N,P-HMCS is closer to 2 owing to the synergistic effect of rich graphitic N site and rich electron-domain C-P bond, while the *n* value of N,S-HMCS tends to 4 due to the combined impact of rich pyridinic N site and indigent electron-domain C-S bond. The differences in the structure and chemistry of N active site in alkaline media affect the chemical rearrangement after the first proton-coupled electron transfer to O₂, further steering the ORR activity and selectivity. These findings provide important guidelines for the synthesis of highly selective, precious metal-free, nitrogen-doped carbon-based catalysts, such as controlling the types of non-metallic heteroatoms and N doping content to tune the strength of covalent bond in active site system, which may be a scalable approach for controlling electrochemical ORR selective pathways.

CRedit authorship contribution statement

Jiarun Cheng: Methodology, Data curation, Formal analysis, Visualization, Writing – original draft. **Chaojie Lyu:** Methodology, Investigation, Data curation, Validation, Writing – original draft. **Hangren Li:** Simulations, Formal analysis. **Jiwen Wu:** Synthesis, Data curation, Formal analysis. **Yue Hu:** Data curation, Formal analysis. **Bin Han:** Data curation, Formal analysis. **Kaili Wu:** Data curation, Formal analysis. **Mirabbos Hojamberdiev:** Writing – review & editing, Formal analysis. **Dongsheng Geng:** Conceptualization, Funding acquisition, Methodology, Validation, Writing – review & editing.

Declaration of Competing Interest

The authors declare that they have no known competing financial interests or personal relationships that could have appeared to influence the work reported in this paper.

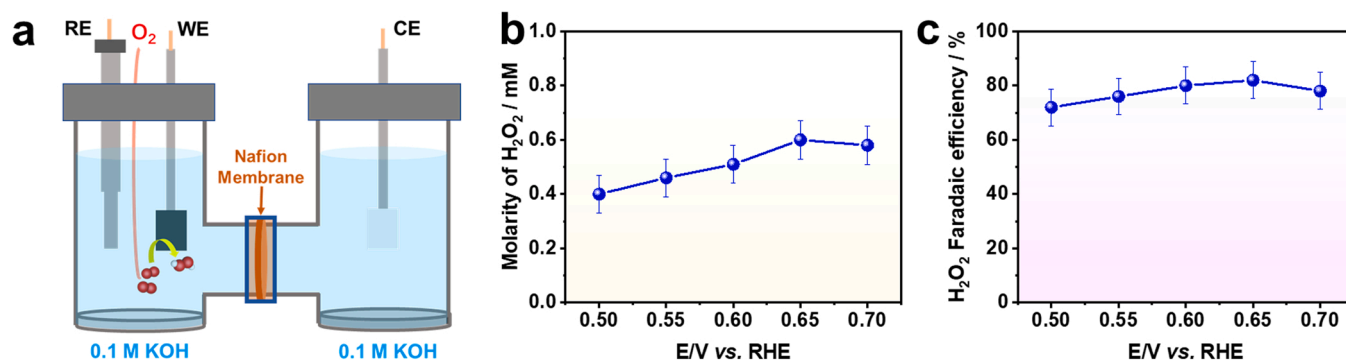


Fig. 9. (a) The schematic illustration of H-cell electrolyzer in O₂-saturated 0.1 M KOH, (b) molarity of H₂O₂ of N,P-HMCS at different potentials, and (c) FE of H₂O₂ electroproduction with 1 h at various applied potentials using the N,P-HMCS electrode in O₂-saturated 0.1 M KOH.

Data availability

Data will be made available on request.

Acknowledgments

This work was supported by the University of Science and Technology Beijing. DG acknowledges the financial support from 111 Project (no. B170003) and Foshan Science and Technology Innovation Project (no. 2018IT100363).

Appendix A. Supporting information

Supplementary data associated with this article can be found in the online version at [doi:10.1016/j.apcatb.2023.122470](https://doi.org/10.1016/j.apcatb.2023.122470).

References

- Z. Zhang, X. Zhao, S. Xi, L. Zhang, Z. Chen, Z. Zeng, M. Huang, H. Yang, B. Liu, S. J. Pennycook, P. Chen, Atomically dispersed cobalt trifunctional electrocatalysts with tailored coordination environment for flexible rechargeable zn-air battery and self-driven water splitting, *Adv. Energy Mater.* 10 (2020) 2002896.
- J. Zhao, C. Fu, K. Ye, Z. Liang, F. Jiang, S. Shen, X. Zhao, L. Ma, Z. Shadike, X. Wang, J. Zhang, K. Jiang, Manipulating the oxygen reduction reaction pathway on Pt-coordinated motifs, *Nat. Commun.* 13 (2022) 685.
- Y. Jia, Z. Xue, J. Yang, Q. Liu, J. Xian, Y. Zhong, Y. Sun, X. Zhang, Q. Liu, D. Yao, G. Li, Tailoring the electronic structure of an atomically dispersed zinc electrocatalyst: coordination environment regulation for high selectivity oxygen reduction, *Angew. Chem. Int. Ed.* 61 (2022) 202110838.
- B. Lv, X. Li, K. Guo, J. Ma, Y. Wang, H. Lei, F. Wang, X. Jin, Q. Zhang, W. Zhang, R. Long, Y. Xiong, U.P. Apfel, R. Cao, Controlling oxygen reduction selectivity through steric effects: electrocatalytic two-electron and four-electron oxygen reduction with cobalt porphyrin atropisomers, *Angew. Chem. Int. Ed.* 60 (2021) 12742–12746.
- J. Hu, W. Liu, C. Xin, J. Guo, X. Cheng, J. Wei, C. Hao, G. Zhang, Y. Shi, Carbon-based single atom catalysts for tailoring the ORR pathway: a concise review, *J. Mater. Chem. A* 9 (2021) 24803–24829.
- T. Zhang, H. Wang, J. Zhang, J. Ma, Z. Wang, J. Liu, X. Gong, Carbon charge population and oxygen molecular transport regulated by program-doping for highly efficient 4e-ORR, *Chem. Eng. J.* 444 (2022), 136560.
- M. Fan, Q. Yuan, Y. Zhao, Z. Wang, A. Wang, Y. Liu, K. Sun, J. Wu, L. Wang, J. Jiang, A facile "Double-Catalysts" approach to directionally fabricate pyridinic N-B-pair-doped crystal graphene nanoribbons/amorphous carbon hybrid electrocatalysts for efficient oxygen reduction reaction, *Adv. Mater.* 34 (2022) 2107040.
- D. He, L. Zhong, S. Gan, J. Xie, W. Wang, Z. Liu, W. Guo, X. Yang, L. Niu, Hydrogen peroxide electrosynthesis via regulating the oxygen reduction reaction pathway on Pt noble metal with ion poisoning, *Electrochim. Acta* 371 (2021), 137721.
- Q. Ji, Y. Zhou, C. Xiang, G. Zhang, J. Li, H. Liu, J. Qu, Manipulation of neighboring palladium and mercury atoms for efficient *OH transformation in anodic alcohol oxidation and cathodic oxygen reduction reactions, *ACS Appl. Mater. Interfaces* 12 (2020) 12677–12685.
- K. Kusunoki, D. Kudo, K. Hayashi, Y. Chida, N. Todoroki, T. Wadayama, Oxygen reduction reaction of third element-modified Pt/Pd(111): effect of atomically controlled ir locations on the activity and durability, *ACS Catal.* 11 (2021) 1554–1562.
- J. Li, M.N. Banis, Z. Ren, K.R. Adair, K. Doyle-Davis, D.M. Meira, Y.Z. Finckro, L. Zhang, F. Kong, T.K. Sham, R. Li, J. Luo, X. Sun, Unveiling the nature of Pt single-atom catalyst during electrocatalytic hydrogen evolution and oxygen reduction reactions, *Small* 17 (2021) 2007245.
- H. Chen, C. Yuan, X. Yang, X. Cheng, A.A. Elzathary, A. Alghamdi, J. Su, X. He, Y. Deng, Hollow mesoporous carbon nanospheres loaded with Pt nanoparticles for colorimetric detection of ascorbic acid and glucose, *ACS Appl. Nano Mater.* 3 (2020) 4586–4598.
- K.M. Nair, V. Kumaravel, S.C. Pillai, Carbonaceous cathode materials for electro-Fenton technology: mechanism, kinetics, recent advances, opportunities and challenges, *Chemosphere* 269 (2021), 129325.
- J.Y. Zhang, G. Zhang, S.Y. Jin, Y.J. Zhou, Q.H. Ji, H.C. Lan, H.J. Liu, J.H. Qu, Graphitic N in nitrogen-Doped carbon promotes hydrogen peroxide synthesis from electrocatalytic oxygen reduction, *Carbon* 163 (2020) 154–161.
- H. Xu, J. Yang, R. Ge, J. Zhang, Y. Li, M. Zhu, L. Dai, S. Li, W. Li, Carbon-based bifunctional electrocatalysts for oxygen reduction and oxygen evolution reactions: optimization strategies and mechanistic analysis, *J. Energy Chem.* 71 (2022) 234–265.
- J. Zhang, Y. Sun, J. Zhu, Z. Kou, P. Hu, L. Liu, S. Li, S. Mu, Y. Huang, Defect and pyridinic nitrogen engineering of carbon-based metal-free nanomaterial toward oxygen reduction, *Nano Energy* 52 (2018) 307–314.
- P. Su, M. Zhou, X. Lu, W. Yang, G. Ren, J. Cai, Electrochemical catalytic mechanism of N-doped graphene for enhanced H₂O₂ yield and in-situ degradation of organic pollutant, *Appl. Catal. B-Environ.* 245 (2019) 583–595.
- E. Contreras, D. Dominguez, H. Tiznado, J. Guerrero-Sanchez, N. Takeuchi, G. Alonso-Nunez, O.E. Contreras, M.T. Oropeza-Guzman, J.M. Romo-Herrera, N-Doped carbon nanotubes enriched with graphitic nitrogen in a buckypaper configuration as efficient 3D electrodes for oxygen reduction to H₂O₂, *Nanoscale* 11 (2019) 2829–2839.
- J.A. Behan, E. Mates-Torres, S.N. Stamatina, C. Domínguez, A. Iannaci, K. Fleischer, M.K. Hoque, T.S. Perova, M. García-Melchor, P.E. Colavita, Untangling cooperative effects of pyridinic and graphitic nitrogen sites at metal-free N-doped carbon electrocatalysts for the oxygen reduction reaction, *Small* 15 (2019) 1902081.
- T. Ishii, M. Philavanh, J. Negishi, E. Inukai, J.-i. Ozaki, preparation of chemically structure-controlled BN-doped carbons for the molecular understanding of their surface active sites for oxygen reduction reaction, *ACS Catal.* 12 (2022) 1288–1297.
- H.-J. Zhang, J. Geng, C. Cai, Z.-F. Ma, Z. Ma, W. Yao, J. Yang, Effect of doping order on metal-free heteroatoms dual-doped carbon as oxygen reduction electrocatalyst, *Chin. Chem. Lett.* 32 (2021) 745–749.
- C. Hu, R. Paul, Q. Dai, L. Dai, Carbon-based metal-free electrocatalysts: from oxygen reduction to multifunctional electrocatalysis, *Chem. Soc. Rev.* 50 (2021) 11785.
- X. Tong, M. Cherif, G. Zhang, X. Zhan, J. Ma, A. Almesrati, F. Vidal, Y. Song, J. P. Claverie, S. Sun, N. P-Codoped, Graphene dots supported on N-doped 3D graphene as metal-free catalysts for oxygen reduction, *ACS Appl. Mater. Interfaces* 13 (2021) 30512–30523.
- S. Cao, W. Shang, G.-L. Li, Z.-F. Lu, X. Wang, Y. Yan, C. Hao, S. Wang, G. Sun, Defect-rich and metal-free N, S co-doped 3D interconnected mesoporous carbon material as an advanced electrocatalyst towards oxygen reduction reaction, *Carbon* 184 (2021) 127–135.
- T. Oh, M. Kim, D. Park, J. Kim, Synergistic interaction and controllable active sites of nitrogen and sulfur co-doping into mesoporous carbon sphere for high performance oxygen reduction electrocatalysts, *Appl. Surf. Sci.* 440 (2018) 627–636.
- J. Wu, X. Zheng, C. Jin, J. Tian, R. Yang, Ternary doping of phosphorus, nitrogen, and sulfur into porous carbon for enhancing electrocatalytic oxygen reduction, *Carbon* 92 (2015) 327–338.
- Y. Xia, H. Shang, Q. Zhang, Y. Zhou, X. Hu, Electrogenation of hydrogen peroxide using phosphorus-doped carbon nanotubes gas diffusion electrodes and its application in electro-Fenton, *J. Electroanal. Chem.* 840 (2019) 400–408.
- Z. Li, A. Kumar, N. Liu, M. Cheng, C. Zhao, X. Meng, H. Li, Y. Zhang, Z. Liu, G. Zhang, X. Sun, Oxygenated P/N co-doped carbon for efficient 2e⁻ oxygen reduction to H₂O₂, *J. Mater. Chem. A* 10 (2022) 14355–14363.

- [29] C. Dong, Q. Yu, R.P. Ye, P. Su, J. Liu, G.H. Wang, Hollow carbon sphere nanoreactors loaded with PdCu nanoparticles: void-confinement effects in liquid-phase hydrogenations, *Angew. Chem. Int. Ed.* 59 (2020) 18374–18379.
- [30] H. Liu, Z. Li, J. Dong, D. Liu, C. Liu, Y. Chi, C. Hu, Polyoxometalates encapsulated into hollow double-shelled nanospheres as amphiphilic nanoreactors for an effective oxidative desulfurization, *Nanoscale* 12 (2020) 16586–16595.
- [31] Z. Cai, L. Li, Y. Zhang, Z. Yang, J. Yang, Y. Guo, L. Guo, Amorphous nanocages of Cu-Ni-Fe Hydr(oxy)oxide prepared by photocorrosion for highly efficient oxygen evolution, *Angew. Chem. -Int. Ed.* 58 (2019) 4189–4194.
- [32] J. Sun, H.T. Wang, J.L. He, Y.J. Tian, Ab initio investigations of optical properties of the high-pressure phases of ZnO, *Phys. Rev. B* 71 (2005), 125132.
- [33] L.Z. Li, R. Qin, H. Li, L.L. Yu, Q.H. Liu, G.F. Luo, Z.X. Gao, J. Lu, Functionalized graphene for high-performance two-dimensional spintronics devices, *ACS Nano* 5 (2011) 2601–2610.
- [34] Z. Li, R. Ma, Q. Ju, Q. Liu, L. Liu, Y. Zhu, M. Yang, J. Wang, Spin engineering of single-site metal catalysts, *Innovation* 3 (2022), 100268.
- [35] Y.Z. Zhang, X. Chen, H. Zhang, X.B. Ge, Screening of catalytic oxygen reduction reaction activity of 2, 9-dihalo-1, 10-phenanthroline metal complexes: the role of transition metals and halogen substitution, *J. Colloid Interface Sci.* 609 (2022) 130–138.
- [36] X. Chen, J.B. Chang, Q. Ke, Probing the activity of pure and N-doped fullerenes towards oxygen reduction reaction by density functional theory, *Carbon* 126 (2018) 53–57.
- [37] S. Li, Y. Wang, Y. Ding, Y. He, Y. Zhang, S. Li, J. Zhang, Y. Chen, Hollow N-doped carbon nanoflowers with nanosheets subunits for electrocatalytic oxygen reduction, *Chem. Eng. J.* 430 (2022), 132969.
- [38] N. Jia, T. Yang, S. Shi, X. Chen, Z. An, Y. Chen, S. Yin, P. Chen, N. F-Codoped, Carbon nanocages: an efficient electrocatalyst for hydrogen peroxide electroproduction in alkaline and acidic solutions, *ACS Sus. Chem. Eng.* 8 (2020) 2883–2891.
- [39] D. San Roman, D. Krishnamurthy, R. Garg, H. Hafiz, M. Lamparski, N.T. Nuhfer, V. Meunier, V. Viswanathan, T. Cohen-Karni, EnGineering Three-dimensional (3D) out-of-plane graphene edge sites for highly selective two-electron oxygen reduction electrocatalysis, *ACS Catal.* 10 (2020) 1993–2008.
- [40] J. Zhang, J. Zhang, F. He, Y. Chen, J. Zhu, D. Wang, S. Mu, H.Y. Yang, Defect and doping Co-engineered non-metal nanocarbon ORR electrocatalyst, *Nano-Micro Lett.* 13 (2021) 65.
- [41] W. Cheng, P. Yuan, Z. Lv, Y. Guo, Y. Qiao, X. Xue, X. Liu, W. Bai, K. Wang, Q. Xu, J. Zhang, Boosting defective carbon by anchoring well-defined atomically dispersed metal-N₄ sites for ORR, OER, and Zn-air batteries, *Appl. Catal. B-Environ.* 260 (2020), 118198.
- [42] Y. Pang, K. Wang, H. Xie, Y. Sun, M.-M. Titirici, G.-L. Chai, Mesoporous carbon hollow spheres as efficient electrocatalysts for oxygen reduction to hydrogen peroxide in neutral electrolytes, *ACS Catal.* 10 (2020) 7434–7442.
- [43] T. Wu, Z. Xu, X. Wang, M. Luo, Y. Xia, X. Zhang, J. Li, J. Liu, J. Wang, H.-L. Wang, F. Huang, Surface-confined self-reconstruction to sulfate-terminated ultrathin layers on NiMo₃S₄ toward biomass molecule electro-oxidation, *Appl. Catal. B-Environ.* 323 (2023), 122126.
- [44] Q. Wu, M. Liu, N. Shang, S. Gao, J. Wang, C. Wang, Z. Wang, H. Wang, Y. Gao, Preparation of N, S co-decorated carbon supported iron species for oxygen reduction and zinc air batteries, *J. Alloy. Compd.* 848 (2020), 156367.
- [45] M.S.A. Sher Shah, J. Lee, A. Rauf, J.H. Park, B. Lim, P.J. Yoo, Electrostatically regulated ternary-doped carbon foams with exposed active sites as metal-free oxygen reduction electrocatalysts, *Nanoscale* 10 (2018) 19498–19508.
- [46] D. Geng, Y. Chen, Y. Chen, Y. Li, R. Li, X. Sun, S. Ye, S. Knights, High oxygen-reduction activity and durability of nitrogen-doped graphene, *Energy Environ. Sci.* 4 (2011) 760–764.
- [47] Y. Wang, W. Peng, J. Wang, G. Chen, N. Li, Y. Song, Z. Cheng, B. Yan, La Hou, S. Wang, Sulfamethoxazole degradation by regulating active sites on distilled spirits lees-derived biochar in a continuous flow fixed bed peroxymonosulfate reactor, *Appl. Catal. B-Environ.* 310 (2022), 121342.
- [48] S.H. Ho, Y.D. Chen, R. Li, C. Zhang, Y. Ge, G. Cao, M. Ma, X. Duan, S. Wang, N. Q. Ren, N-doped graphitic biochars from C-phycocyanin extracted Spirulina residue for catalytic persulfate activation toward nonradical disinfection and organic oxidation, *Water Res* 159 (2019) 77–86.
- [49] H. He, D. Huang, Y. Tang, Q. Wang, X. Ji, H. Wang, Z. Guo, Tuning nitrogen species in three-dimensional porous carbon via phosphorus doping for ultra-fast potassium storage, *Nano Energy* 57 (2019) 728–736.
- [50] T. Zhang, J. Wu, Z. Wang, Z. Wei, J. Liu, X. Gong, Transfer of molecular oxygen and electrons improved by the regulation of C-N/C=O for highly efficient 2e-ORR, *Chem. Eng. J.* 433 (2022), 133591.
- [51] Y. Hu, J. Zhang, T. Shen, Z. Li, K. Chen, Y. Lu, J. Zhang, D. Wang, Efficient electrochemical production of H₂O₂ on hollow N-doped carbon nanospheres with abundant micropores, *ACS Appl. Mater. Interfaces* 13 (2021) 29551–29557.
- [52] B. Huang, Y. Liu, X. Huang, Z. Xie, Multiple heteroatom-doped few-layer carbons for the electrochemical oxygen reduction reaction, *J. Mater. Chem. A* 6 (2018) 22277–22286.
- [53] M. Fan, Y. Huang, F. Yuan, Q. Hao, J. Yang, D. Sun, Effects of multiple heteroatom species and topographic defects on electrocatalytic and capacitive performances of graphene, *J. Power Sources* 366 (2017) 143–150.
- [54] S. Dou, A. Shen, Z. Ma, J. Wu, L. Tao, S. Wang, N-, P- and S-tridoped graphene as metal-free electrocatalyst for oxygen reduction reaction, *J. Electroanal. Chem.* 753 (2015) 21–27.
- [55] A. Mulyadi, Z. Zhang, M. Dutzer, W. Liu, Y. Deng, Facile approach for synthesis of doped carbon electrocatalyst from cellulose nanofibrils toward high-performance metal-free oxygen reduction and hydrogen evolution, *Nano Energy* 32 (2017) 336–346.
- [56] H.-J. Niu, A.-J. Wang, L. Zhang, J.-J. Guo, J.-J. Feng, Ultrafine NiCoP-decorated N, S,P-codoped hierarchical porous carbon nanosheets as an efficient bifunctional electrocatalyst for oxygen reduction and oxygen evolution, *Mat. Chem. Front.* 3 (2019) 1849–1858.
- [57] N.-b Huang, J.-j Zhang, Y. Sun, X.-n Sun, Z.-y Qiu, X.-w Ge, A non-traditional biomass-derived N, P, and S ternary self-doped 3D multichannel carbon ORR electrocatalyst, *New J. Chem.* 44 (2020) 14604–14614.
- [58] J. Wang, Y. Liu, N. Li, F. Qin, F. Xu, W. Shi, H. Li, W. Shen, N. Petal-like, O-codoped carbon nanosheets as Mott-Schottky nanoreactors in electrodes of Zn-Air batteries and supercapacitors, *Carbon* 178 (2021) 581–593.
- [59] J.Y. Cheon, J.H. Kim, J.H. Kim, K.C. Goddeti, J.Y. Park, S.H. Joo, Intrinsic relationship between enhanced oxygen reduction reaction activity and nanoscale work function of doped carbons, *J. Am. Chem. Soc.* 136 (2014) 8875–8878.
- [60] Y. Cai, L. Tao, G. Huang, N. Zhang, Y. Zou, S. Wang, Regulating carbon work function to boost electrocatalytic activity for the oxygen reduction reaction, *Chin. J. Catal.* 42 (2021) 938–944.
- [61] L. Lai, J.R. Potts, D. Zhan, L. Wang, C.K. Poh, C. Tang, H. Gong, Z. Shen, J. Lin, R. S. Ruoff, Exploration of the active center structure of nitrogen-doped graphene-based catalysts for oxygen reduction reaction, *Energy Environ. Sci.* 5 (2012) 7936–7942.
- [62] X. Yang, Y. Zeng, W. Alnough, Y. Hou, D. Higgins, G. Wu, Tuning two-electron oxygen-reduction pathways for H₂O₂ electrosynthesis via engineering atomically dispersed single metal site catalysts, *Adv. Mater.* 34 (2022) 2107954.
- [63] H. Zhao, Z.Y. Yuan, Design strategies of non-noble metal-based electrocatalysts for two-electron oxygen reduction to hydrogen peroxide, *ChemSusChem* 14 (2021) 1616–1633.
- [64] Y. Zheng, X. Xu, J. Chen, Q. Wang, Surface O²⁻ regulation on POM electrocatalyst to achieve accurate 2e/4e-ORR control for H₂O₂ production and Zn-air battery assemble, *Appl. Catal. B-Environ.* 285 (2021), 119788.
- [65] H. Sun, P. Zhou, X. Ye, J. Wang, Z. Tian, Z. Zhu, C. Ma, W. Liang, A. Li, Nitrogen-doping hollow carbon nanospheres derived from conjugated microporous polymers toward oxygen reduction reaction, *J. Colloid Interface Sci.* 617 (2022) 11–19.
- [66] X. Sun, J. Xu, Y. Ding, B. Zhang, Z. Feng, D.S. Su, The effect of different phosphorus chemical states on an onion-like carbon surface for the oxygen reduction reaction, *ChemSusChem* 8 (2015) 2872–2876.
- [67] H. Shin, N. Kang, D. Kang, J.S. Kang, J.H. Ko, D.H. Lee, S. Park, S.U. Son, Y.-E. Sung, Understanding the roles of sulfur dopants in carbonaceous electrocatalysts for the oxygen reduction reaction: the relationship between catalytic activity and work function, *ChemElectroChem* 5 (2018) 1905–1913.
- [68] K. Wang, Q. Dai, C. Hu, Y. Tong, Y. Wang, S. Song, L. Dai, Earth-abundant metal-free carbon-based electrocatalysts for Zn-air batteries to power electrochemical generation of H₂O₂ for in-situ wastewater treatment, *Chem. Eng. J.* 416 (2021), 128338.
- [69] H.W. Kim, V.J. Bukas, H. Park, S. Park, K.M. Diederichsen, J. Lim, Y.H. Cho, J. Kim, W. Kim, T.H. Han, J. Voss, A.C. Luntz, B.D. McCloskey, Mechanisms of two-electron and four-electron electrochemical oxygen reduction reactions at nitrogen-doped reduced graphene oxide, *ACS Catal.* 10 (2019) 852–863.
- [70] D.B. Sepa, M.V. Vojnovic, A. Damjanovic, Kinetics and mechanism of O₂ reduction at Pt in alkaline solutions, *Electrochim. Acta* 25 (1980) 1491–1496.
- [71] N. Ramaswamy, S. Mukerjee, Fundamental mechanistic understanding of electrocatalysis of oxygen reduction on Pt and non-Pt surfaces: acid versus alkaline media, *Adv. Phys. Chem.* 2012 (2012) 1–17.
- [72] N. Ramaswamy, S. Mukerjee, Influence of inner- and outer-sphere electron transfer mechanisms during electrocatalysis of oxygen reduction in alkaline media, *J. Phys. Chem. C* 115 (2011) 18015–18026.
- [73] T. Shen, X. Huang, S. Xi, W. Li, S. Sun, Y. Hou, The ORR electron transfer kinetics control via Co-N and graphitic N sites in cobalt single atom catalysts in alkaline and acidic media, *J. Energy Chem.* 68 (2022) 184–194.
- [74] S. Siahrostami, S.J. Villegas, A.H. Bagherzadeh Mostaghimi, S. Back, A.B. Farimani, H. Wang, K.A. Persson, J. Montoya, A review on challenges and successes in atomic-scale design of catalysts for electrochemical synthesis of hydrogen peroxide, *ACS Catal.* 10 (2020) 7495–7511.
- [75] J. Zhang, H. Zhang, M.J. Cheng, Q. Lu, Tailoring the electrochemical production of H₂O₂: strategies for the rational design of high-performance electrocatalysts, *Small* 16 (2020) 1902845.
- [76] J. Woo, J.S. Lim, J.H. Kim, S.H. Joo, Heteroatom-doped carbon-based oxygen reduction electrocatalysts with tailored four-electron and two-electron selectivity, *Chem. Commun.* 57 (2021) 7350–7361.